NTNU
Norwegian University of
Science and Technology

Solid Stress and Nanoparticle Microdistribution in Xenografts: Effects of Ultrasound and Microbubble Cavitation

Ingunn Hanson

Nanotechnology
Submission date: July 2018
Supervisor: Catharina de Lange Davies, IFY

Norwegian University of Science and Technology
Department of Physics

Abstract

A drug delivery system (DDS) was characterized for two different xenografts in mice: OHS and PC3. Nanoparticles (NP) encapsulating fluorescent model drugs were used as stabilizing shells around gas microbubbles (MB), and ultrasound (US) was used to locally cavitate and collapse the MBs at the tumor site. MB cavitation is known to induce several effects which are beneficial for NP drug delivery, causing increased accumulation, extravasation and extracellular matrix (ECM) penetration by the NPs. These effects all contribute to a higher tumor specificity and ability to reach all tumor cells, allowing for a safer and more efficient method of cancer treatment.

Frozen tumor sections were imaged using confocal laser scanning microscopy (CLSM), and analyzed in terms of NP microdistribution. The distribution of solid stress (SS) in the tumors was characterized using the "Planar cut" method and subsequent US imaging. Tile scans from frozen tumor sections were fitted to surface plots (SP) of SS distribution in the same tumor, and a connection between SS levels and NP microdistribution was established.

The baseline enhanced permeability and retention (EPR) effect of both tumor models was established, and found significantly higher for OHS tissue: the NP accumulation was 64.9 % higher, the NP extravasation was 50.3 % higher, and the ECM penetration was 35.2 % higher in OHS tissue ($p=0.01$, $p<0.0001$ and $p<0.0001$, respectively, t-test). The DDS with US proved to be more effective for tissue with a lower baseline EPR effect.

SS distribution was shown to be highly heterogeneous between tumors, and the level of SS was significantly higher in OHS than in PC3 tumors, by 99.5 % ($p<0.0001$, t-test). For the first time, it was shown that treatment with US induced MB collapse lowered the SS in both tumor models: by 11.1 % in OHS tumors and 8.8 % in PC3 tumors ($p=0.029$ and $p=0.030$, respectively, t-test).

The correlation between SS levels and NP microdistribution was heterogeneous. PC3 tumors showed no effect of the US treatment on the correlation between SS level and NP accumulation, extravasation or ECM penetration, which were all negative for both groups. OHS tumors, on the other hand, experienced a change from positive to negative correlation between SS level and NP accumulation, and a change from no correlation to a positive correlation between SS level and NP extravasation after treatment.

Sammendrag

Et system for å levere medisin ble karakterisert i to forskjellige xenografter i mus, OHS og PC3. Nanopartikler (NP) som inneholdt fluorescerende modellmedisiner ble brukt som et stabiliserende skall rundt mikrobobler (MB) av gass, og ultralyd (US) ble brukt til å lokalt kavitere og indusere kollaps av MBs ved svulsten. Kavitasjon av MBs er kjent for å forårsake flere effekter som kan være fordelaktige for medisinleveranse via NPs, og som øker NPs evne til å akkumuleres, ekstravaseres og til å penetrere den ekstracellulære matriksen (ECM). Disse effektene bidrar til en høyere tumorspesifisitet og evne til å nå ut til alle cellene i svulsten, noe som legger til rette for en tryggere og mer effektiv måte å behandle kreft på.

Frosne tumorsnitt ble avbildet med konfokalmikroskop og analysert med hensyn til mikrodistribusjon av NPs. Distribusjonen av fast spenning (SS) i tumorene ble kartlagt ved hjelp av "Planar cut"-metoden og ultralydavbilding. Skanninger av komplette tumorsnitt ble tilpasset overflateplott som viste distribusjonen av SS i samme svulst, og sammenhengen mellom nivået av SS og mikrodistribusjonen av NPs ble kartlagt.

Effekten med økt permeabilitet og forvaring (EPR-effekt) i tumorer var opprinnelig større for OHS enn for PC3: akkumuleringen av NPs var 64,9% høyere, ekstravaseringen av NPs var 50,3% høyere, og ECM-penetrasjonen var 35,2% høyere i OHS-tumorer ($p=0{,}01$, $p<0{,}0001$ og $p<0{,}0001$, respektivt, t-test). Medisinsystemet med ultralyd viste seg å være mer effektivt i svulster som i utgangspunktet hadde en lavere EPR-effekt.

Distribusjonen av SS viste seg å være svært heterogen mellom forskjellige svulster, og nivået av SS var signifikant 99,5% høyere i OHS- enn i PC3-tumorer ($p<0{,}0001$, t-test). For første gang ble det vist at behandling med US-indusert kollaps av MBs senket nivået av SS i begge tumormodellene, med 11,1% i OHS-tumorer og 8,8% i PC3-tumorer ($p=0{,}029$ og $p=0{,}030$, respektivt, t-test).

Korrelasjonen mellom nivå av SS og mikrodistribusjon av NPs var heterogen. PC3-tumorer viste ingen effekt av US-behandlingen når det gjaldt korrelasjon mellom NPs evne til akkumuleres, ekstravaseres eller til å penetrere ECM og nivå av SS. Denne korrelasjonen var negativ for begge gruppene. OHS-tumorene derimot, gikk fra positiv til negativ korrelasjon mellom nivå av SS og akkumulering av NPs, og fra ingen til positiv korrelasjon mellom nivå av SS og ekstravasering av NPs etter behandlingen.

Preface

This thesis is the conclusion to my 5 years at the Nanotechnology program at the Norwegian University of Science and Technology. For the last three years, I have specialized in bionanotechnology, and I was lucky to be able to join Catharina de Lange Davies' group working with ultrasound and delivery of drugs and nanoparticles, at the Institute of Physics, Division of Biophysics and Medical Technology. I have conducted both my 5th year Specialization project and my Master's project as a part of this group, and would like to express my gratitude for this opportunity.

First, I would like to thank Einar Sulheim and Catharina de Lange Davies for their guidance, help and support throughout this project. I would also like to express my gratitude to Sofie Snipstad for training in cell culture and help during animal trials. I am also very thankful to Astrid Bjørkøy for microscope training and for always taking the time to answer my questions. I would like to thank Stein Martin Fagerland for help with ultrasound imaging. For the provision of nanoparticle microbubble-complexes; I would like to thank Anne Rein Hatletveit at SINTEF, and for sectioning frozen tumors; Ingunn Nervik at CMIC NTNU. Finally, I would like to thank Aleksander Jacobsen for his help with coding, and for always helping me get out of bed in the morning.

List of abbreviations

A – Amplitude
AFM – Atomic Force Microscopy
ARF – Acoustic Radiation Force
AU – Airy Unit
BBB – Blood Brain Barrier
CD31 – Cluster of Differentiation 31
CLSM – Confocal Laser Scanning Microscopy
CW – Continuous Wave
DAPI – 4',6-diamidino-2-phenylindole
DDS – Drug Delivery System
DF – Duty Fraction
DLS – Dynamic Light Scattering
DMEM – Dulbecco's Modified Eagle Medium
DOF – Depth Of Field
ECM – Extracellular Matrix
EPR – Enhanced Permeability and Retention
f – frequency
FBS – Fetal Bovine Serum
FIJI – Fiji Is Just ImageJ
HA – Hyaluronic Acid
HR – High Resolution
IFP – Interstitial Fluid Pressure
MB – Microbubble
MI – Mechanical Index
NA – Numerical Aperture
NP – Nanoparticle
NPMB – Nanoparticle Microbubble
OHS – Human Osteosarcoma
PBS – Phosphate Buffered Saline
PCC – Pearson Correlation Coefficient
PC3 – Human Prostatic Adenocarcinoma
PEBCA – poly(ethyl-butyl cyanoacrylate)
PEG – Polyethylene Glycol
PFP – Perfluorpropane
PMT – Photomultiplier Tube
PRF – Pulse Repetition Frequency
PRP – Pulse Repetition Period
PW – Pulsed Wave
RES – Reticuloendothelial System
ROI – Region Of Interest
RPMI – Roswell Park Memorial Institute
SD – Standard Deviation
SEM – Scanning Electron Microscope
SHG – Second Harmonic Generation
SP – Surface Plot
SPL – Spatial Pulse Length
SS – Solid Stress
T – Period
TSG – Tumor Supressor Gene
US – Ultrasound
WLI – White Light Interferometry
Z – Impedance
λ – wavelength

Contents

Chapter 1

Introduction

Every year, millions of people receive a cancer diagnosis from their doctor. For these patients and their families and friends, these news are most likely devastating. Despite progress in recent years, cancer is still a deadly disease for about 8 million patients each year, according to the Global Cancer Observatory [1]. Cancer is a highly diverse illness. The differences between types of cancer are significant, and even one type of cancer can vary greatly in development, spreading, and treatment susceptibility from patient to patient. This means that the universal "cure for cancer" is outside the reach of today's scientists.

Today, cancer treatment in itself is intensely stressful and painful for many patients. Chemotherapeutic treatment is often the best option, but it provides sub optimal results and serious side effects [2]. This is mainly because of the lack of specificity shown by chemotherapeutic drugs, meaning that healthy cells will be killed along with cancer cells.

The last few decades, a new solution to some of the problems associated with chemotherapeutic treatment of cancer has emerged in designing complete drug delivery systems (DDS). These systems intend increase the probability that the drugs are delivered to their intended target, thus increasing effect and decreasing side effects of the therapy

The emerge of nanotechnology have further improved possibilities for safe delivery of drugs to specific areas, like tumors. Drugs can be encapsulated inside or attached to the surface of nanoparticles (NP) [3], a method which both increases their chance of reaching the tumor, and decreases their chance of accumulating in healthy tissue. When hydrophobic drugs are protected by NPs, their circulation time in the blood is increased, allowing them to reach their target more easily [4]. To further increase circulation time of the NPs, they can be coated with polyethylene glycol (PEG), a technique which makes them 'invisible' to the immune system [5].

To prevent the NPs from accumulating in healthy tissue, passive or active targeting can be applied. The most popular form of passive targeting is to exploit the enhanced permeability and retention (EPR) effect [6]. This method is based on the inherent properties of solid tumors where blood vessels have larger endothelial

openings than healthy vasculature [7], meaning NPs of the right size can escape tumor vasculature, but not healthy vasculature. However, this effect has shown poor ability to translate into the clinic.

In this thesis, a NP based DDS designed with the intention of enhancing the EPR effect through active targeting using focused ultrasound (US), was characterized. The system was based on PEGylated NPs with fluorescent model drugs used as stabilizing shells around gas microbubbles (MB). Focused US at the tumor location caused MB cavitation and collapse, forcibly spreading NPs in the target area. In addition, effects like shear forces and microjets from the MB collapse have been shown to increase the vascular permeability and improve NP transport through the extracellular matrix (ECM) [8, 9, 10].

The system described above has already been shown to increase delivery to the tumor and decrease accumulation in healthy tissue [11]. However, because of the enormous variability between tumor types, there was a need to investigate the effect of the DDS with US in several types of tumor tissue. In addition, previous papers have indicated that the NPs in this DDS were heterogeneously distributed within the tumor tissue [12]. Therefore, the focus of the characterization process described in this thesis, was inter- and intra-tumoral heterogeneity, and the possible causes behind this.

To investigate inter-tumoral heterogeneity, the microdistribution of NPs was characterized in two tumor tissues with different properties in terms of vascularization and cell density, among others. High resolution (HR) confocal light scanning microscopy images (CLSM) of tumors that received treatment, were compared to images of control tumors, for both tumor types. The parameters NP accumulation, extravasation and ECM penetration were quantified, as these are important in drug delivery.

To investigate intra-tumoral heterogeneity, a new method of measuring solid stress (SS) within tumors [13] was used. SS was chosen as a parameter of intra-tumoral heterogeneity because it has previously been difficult to measure, and therefore poorly characterized. The SS distribution was mapped for independent tumors, and the microdistribution of drug loaded NPs was quantified for the same tumors, in order to relate NP accumulation, extravasation and distribution to SS level.

By understanding the mechanisms behind the microdistribution of NPs in tumor tissue, this particular DDS with US can be evaluated and further improved. In turn, this could contribute to a less painful, safer and more effective treatment option for cancer patients.

This Master's project is a continuation of the Specialization Project "Nanoparticle microdistribution in tumor tissue: a characterization of a drug delivery system based on microbubble cavitation" by the same author (2017). It is therefore inevitable that there is some overlap between the two thesis, especially in the "Theory" and "Methods" chapters. As the two projects concerned many of the same characteristics of the DDS for two different tumor models, it was also natural to compare the results from the Specialization Project to the results presented in this thesis. The results from the Specialization project are summarized in Section 4.1.

Chapter 2

Theory

2.1 Cancer

2.1.1 The cellular biology of cancer

The growth and expansion of tissue is a process which is normally strictly regulated. Tissue growth can occur via two different processes, called hypertrophy and hyperplasia. In hypertrophy, each component, or cell, experiences an increase in size. Muscle growth as a result of physical exercise is an example of hypertrophy. Hyperplasia is an increase in the number of cells. This is the result of cell proliferation, a process where cells in the tissue divide and become two separate cells [14]. Hyperplasia is seen for example where there is damage to a tissue which causes it to regrow. In healthy tissue, this process stops when the tissue is regrown.

To proliferate, cells need to divide. Cell division is regulated through the cell cycle, ending in a final step called mitosis. During the cycle, the DNA of the cell is replicated, and the membrane breaks to create two individual cells [14]. To ensure that only cells with undamaged DNA undergo mitosis, several checkpoints exist throughout the cell cycle. In non-cancerous cells, any errors detected in these checkpoints will cause the cell to undergo apoptosis, or programmed cell death.

Tumor tissue differs from healthy tissue in the regulation of proliferation and apoptosis. The changes to these processes are the result of several mutations in the tumor cell's DNA. The two main types of DNA mutations observed in tumor cells are those of oncogenes and tumor suppressor genes (TSGs). When a gene with the possibility to create cancer, a proto-oncogene, mutates, it can become an oncogene [15]. On the other hand, TSGs normally prevents tumor development by encoding proteins important in for example DNA repair or cell cycle check points. A mutation that causes a TSG to lose it's function will promote cancer development [16].

Development of oncogenes and loss of function in TSGs leads to the formation of tumors: While healthy cells will proliferate when needed, tumor cells will not stop proliferating. In addition, most, if not all, tumor cells have faulty checkpoints in the cell cycle, preventing the cell from undergoing apoptosis [14]. A third difference

between healthy cells and tumor cells is the level of telomerase activity within the cell. Telomerase is an enzyme ensuring continued renewal of the telomeres at the end of the cell's chromosomes. Without constant renewal of the telomeres, a cell will undergo a limited number of divisions before dying. The high level of telomerase in tumor cells compared to healthy cells ensure that they can undergo an unlimited number of divisions. This is referred to as the replicative immortality of tumor cells [17]. The result of these deviations from healthy cells is a cell dense tissue, which is what we call a tumor.

Tumors are divided into three types: benign, *in situ*, and malignant tumors. Benign tumors do not spread. The only damages caused by these tumors are pressure or obstruction of the surrounding tissue, depending on their placement. *In situ* tumors arise in the epithelium and have the appearance of cancer cells, but does not invade the underlying basement membrane to spread. Malignant tumors, or cancer, have the ability to invade the basement membrane to spread to other tissues. By entering the blood stream, tumor cells are able to relocate within the organism and subsequently attach to a new site, to grow a new tumor there. This is known as the creation of metastases, or secondary tumors.

An important characteristic of cancer cells is the ability to signal for blood vessel growth, or angiogenesis [14]. Tumor cells, like all cells, need oxygen and nutrients to survive and to proliferate. These necessities, along with the possibility of waste product removal, are provided by the blood vessel network. Therefore, as a tumor grows, it needs to be able to grow new blood vessels to provide access to the blood vessel network throughout the tumor. A tumor without the ability of angiogenesis cannot grow above 1-2 mm in size.

To signal the need for new blood vessels, cells can emit signal molecules called angiogenic growth factors. These factors cause capillary microvessels to form as "sprouts" from existing blood vessels, growing towards the cells emitting the signals. In tumors, these newly formed vessels are highly disorganized and consist of endothelial cells with a morphology that differs from those of normal vessels. In addition, the supporting basement membrane of the new vessels are often incomplete, leading to a characteristic leakiness of the vessels [18]. The continuous growth and accompanying angiogenesis of tumors means that they are perforated by irregular and leaky blood vessels. This in turn leads to a higher degree of extravasation from blood vessels in tumors compared to those in healthy tissue.

In summary, Hanahan and Weinberg [17] assembled six distinct biological functions of all malignant tumor cells termed "The hallmarks of cancer", which was later expanded with four "emerging" hallmarks:

1. The ability to sustain proliferative signalling
2. Evasion of growth supressors
3. Invasion and metastasis
4. Enabling of replicative immortality
5. Angiogenesis induction

6. Resistance to cell death
7. Degeneration of cellular genetics
8. Avoiding destruction by the immune system
9. Genomic instability
10. Tumor-promoting inflammation

2.1.2 Tumor heterogeneity

The hallmarks of cancer described in the previous section are important common characteristics of all cancer cells, but cancer is a disease with enormous variability. Cancer types differ according to the tissue which they originated in to the point that they could be seen as different illnesses. For example, consider Leukemia, or cancer of blood cells, as opposed to a gastrointestinal malignant tumor. These two diseases are both cancer, but have completely different symptoms, risk factors, treatments and outcomes. Even within the same cancer type, the disease can differ based on the cause. For example, virally induced squamous cell cancer of the head and neck differs from the tobacco-induced variant [19]. In addition, the same cancer type will appear differently in different patients, establishing the need for individualized treatment.

The heterogeneity of cancer is also pronounced when looking at different tumors within the same individual. Specifically, metastatic tumors have been proven to possess different characteristics from the primary tumor [19]. This introduces yet another challenge for clinicians, as the treatment needs to be adapted to both primary and any metastatic tumors. The last level of tumor heterogeneity, which is also the one most relevant for the project described in this thesis, is the heterogeneity within a single tumor. An example which will be investigated in this project is the distribution of blood vessels within the tumor mass, typically with more functioning blood vessels in the periphery of the tumor.

2.1.3 Solid stress and interstitial fluid pressure in tumors

Two defining characteristic of tumor cells are the increased proliferation and decreased apoptosis, which makes tumors more cell dense than healthy tissue. The result of the increased density of cells in tumors is a tissue with a high level of stress. In tumors it is conventional to differ between the components of stress resulting from solid structures and from fluids. The stress resulting from solid components in tumor tissue is called solid stress (SS). One component of SS arises from a combination of cancer cells, healthy cells, collagen, hyaluronic acid (HA) and other solid components of the tumor pressing on each other and elevating the internal stress levels. In addition, one component of the SS arises from the tumor tissue pressing against the confinement of the surrounding healthy tissue [20]. These different components are called residual and external components of SS, and both have a significant impact on the internal level of SS in tumors [13].

Healthy tissue does not experience significant levels of SS [13]. In tumors, the presence of compressive SS can lead to collapse of blood and lymphatic vessels, which in turn reduces blood flow in the tumor, thereby limiting the access of nutrients, immune system components, and systemically injected therapeutic drugs [20].

As mentioned earlier, tumors have a high level of angiogenesis, with the result that the vasculature in most tumors is disorganized and leaky [18]. This leakiness is probably the cause of the stress component in tumors arising from fluids: interstitial fluid pressure (IFP). High levels of IFP are seen in tumors partially because of increased leakage from blood vessels with insufficient basement membranes, and partially because of an insufficient lymphatic network, unable to drain all excess fluid from the tumor. The effects of this phenomenon on NP drug delivery will be discussed in Section 2.2.2.

2.1.4 Animal models of cancer

In medical research, model systems of different diseases are necessary to understand disease paths and develop treatment. In cancer research, animal models have long been indispensable, and will continue to be so until a better model system is invented. Although no animals can replicate the conditions of a human body in an exact way, several species have important resemblances that can be exploited in research.

In cancer research, the mouse is the most used animal model. There are several reasons behind this choice, for example similarities in signalling pathways, including those that are involved in tumor development [21]. In addition, several different strains of mice with different characteristics adapted to cancer research are available. For example, transgenic mice are genetically engineered mice that spontaneously develop cancer because of expression of oncogenes or knockout of TSGs. These strands of mice are valuable in researching gene mutations in cancer development, the connection between individual mutations that lead to cancer, and the complexity of cancer development [21].

Another mouse model commonly used, including in the project described in this thesis, is the immunodeficient nude mouse mutant. This mouse strand does not experience an immune reaction to human cells, meaning human cancer strands can be used with the model. Although it can be argued that transgenic mice with spontaneously developing tumors offer a more realistic tumor model, implanting human tumor models into immunodeficient mice can make the characterization process easier and allows for the use of actual human cell lines.

When injecting human tumors into a mouse model, a suspension containing anywhere between 10^6 and 10^7 cells from the desired cell line is injected in the animal, usually subcutaneously into for example the hind leg. This secures easy access to the tumor for subsequent characterization [21]. The tumor is left to grow for days or weeks, while the animal is supervised with regards to overall health and well being. Animal trials are heavily regulated through national and international laws, to ensure animal suffering is kept at the lowest level possible.

2.1.5 Chemotherapy

To treat cancer, the activity and continued growth of the cancer cells need to be stopped. Chemotherapeutic treatment can be used alone, or in combination with surgery or radiotherapy, and it is therefore one of the most common methods to treat cancer. Chemotherapy is the term used about all drugs that are cytotoxic, e.g. they have the ability to kill cells. Most such drugs affect the cell's DNA or associated processes. As of today, it is unavoidable that the chemotherapeutic drugs affect and kill healthy cells as well as tumor cells. The tissues with the highest cell turnover are the most heavily affected, including bone marrow, skin, hair follicles and gastrointestinal mucosa [2].

The fact that the chemotherapeutics used to treat cancer also kills healthy cells, inevitably leads to severe side effects of the treatment. Early side effects include nausea, diarrhea and inflammation of the digestive tract, hair loss, myelosupression (decreased activity of the bone marrow), neurotoxicity (affecting the peripheral nerve system), and nephrotoxicity. Late side effects include cardiotoxicity, acute leukemia, infertility, premature menopause, and lung tissue scarring. In other words, the side effects of chemotherapy are many and severe. In an attempt to limit the side effects, doses of chemotherapeutics are administered at time intervals that will allow healthy tissue to repair the DNA damage caused by the drugs. This is possible because healthy tissue normally has better mechanisms for repairing DNA damage than tumor tissue, creating a balance where the healthy tissue will have time to recover, while the tumor tissue will not. However, differences between cancer types and patient to patient heterogeneity makes determination of dose size and intervals challenging, and with today's chemotherapy, severe side effects are unavoidable [2].

2.2 Nanoparticle drug delivery

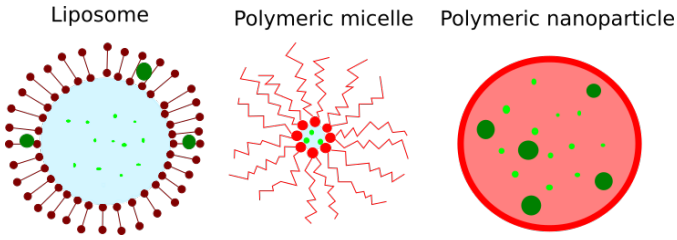

Figure 2.1: Illustration of three common types of nanocarriers used in drug delivery. From left: liposomes, micelles, and polymeric NPs (in green). Liposomes can carry different types of agents like drugs or fluorophores: hydrophilic agents in the aqueous core, and hydrophobic agents in the liposome shell. Polymeric NPs can usually carry different agents. Illustration by the author.

Special systems designed to deliver drugs is one approach to increasing the therapeutic effect and decreasing the side effects of several drugs. Such DDSs can for example be based on NPs. Using NPs in drug delivery to tumors is promising largely because of the many different opportunities for designing and customizing different systems: type of NP, surface chemistry, drug loading ability, targeting, and functionality are all parameters that can be designed to fit a specific need. Even though many DDSs based on NPs have shown success *in vitro*, the success has not been seen *in vivo*, and there has not been much clinical translation of the systems. One of the reasons for this is the still low tumor uptake of NP drug carriers [22].

Virtually any nanosized container can be used as a carrier in a DDS, but some have proven to be more satisfactory than others, and thus are more used today. Among these are micelles, liposomes and polymer NPs, all of which are illustrated in Figure 2.1. The carriers used in this project were polymer NPs. It is worth noting that although "nanosized" strictly speaking requires at least one dimension between the size of 1 and 100 nm, the term is extensively used of objects with at least one dimension below 500 nm [23].

For a nanocarrier in a DDS to be successful, several requirements must be fulfilled. First, the carrier must be safe, i.e. its biocompatibility must be high and it must have a safe route of clearance from the body once it had fulfilled its purpose. Second, for the carrier to have the intended therapeutic effect, the process of drug release should be predictable, and the drug release should preferably be sustained. Furthermore, the fabrication process must meet the relevant practical and economical requirements.

The possible advantages of using nanosized carriers to deliver drugs are many. Hydrophobic drugs prone to accumulate in tissue can be given a longer circulation time when protected by hydrophilic or amphiphilic carriers. The size of NPs is also ideal to prolong the time before a substance is cleared by the body: too big to be cleared by the kidneys [24] but too small to be rapidly detected and removed by

the reticuloendothelial system (RES) [25], they avoid detection for a longer time than free therapeutic molecules. Indeed, NPs can be made virtually undetectable for the immune system by coating them in hydrophilic molecules like polyethylene glycol (PEG) [26], further increasing the circulation time of the drugs.

Another attractive feature of DDSs based on nanosized carriers, is the possibility of targeting the NPs to the intended location, for instance the tumor. Either by passive targeting through the EPR effect, described in Section 2.2.2, or by active targeting, the amount of drugs that end up at the tumor site can be increased, while at the same time reducing the amount accumulating in other parts of the body. Active targeting of NPs can involve ligands or antibodies responding to molecules secreted by the tumor [4], or, as in this project, an externally applied method of targeting, such as US.

2.2.1 Barriers to nanoparticles in drug delivery

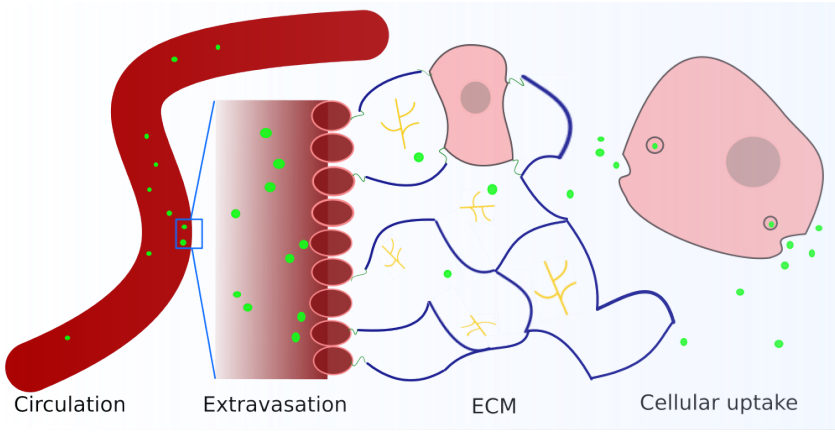

Figure 2.2: Illustration of the barriers to NPs in drug delivery, as described in this section. From left: circulation, extravasation, transport through the ECM, cellular and nuclear uptake. NPs in green. Illustration by the author.

For any drug, there are several obstacles to be overcome before the drug can perform it's intended effect on the target cell. An intravenously administered drug must travel through the blood stream to the target tissue, extravasate the blood vessel, navigate the ECM and be taken up by the cell. These barriers are illustrated in Figure 2.2. A discussion of the importance of each of the barriers for NPs in drug delivery follows:

Circulation The barrier of circulation is a question of allowing the NPs to stay inside the blood vessels long enough to reach the target location without being removed by the host organism. While most NPs used to carry therapeutic molecules are large enough to avoid renal clearance (e.g >8 nm) [24], clearance by the immune system pose a more significant threat. In principle, any foreign

object entering the human body is marked for destruction by the immune system. The human body has several complex systems with this intention, depending on the object and its location, among other factors. NPs are most often marked for destruction via the attachment of opsonins, or antibodies, to the surface of the particles. This process alerts macrophages that the NPs should be targeted and removed [26].

To avoid opsonization and subsequent removal, it has been successful to coat NPs with hydrophilic molecules, such as PEG, before administration. The coating shields or hides the NPs from the immune system and allows them to circulate in the blood vessels for a prolonged time [5, 26].

Once the NPs have reached the tumor location, the tumor vasculature itself can prove a challenge. As explained in Section 2.1, the tumor continuously signals for the construction of more vasculature while it is growing [18]. This causes the blood vessel network to become disorganized, heterogeneous and even incomplete in parts of the tumor [27]. In addition, the high IFP inside the tumor can cause blood vessels to collapse and become non-functional. The total effect is that parts of the tumor may become inaccessible for the NPs, and they may not be able to deliver drugs there.

An advantage of NP drug delivery as opposed to administration of free drugs is the ability to capsule hydrophobic drugs in hydrophilic or amphiphilic containers. As hydrophobic substances tend to accumulate in tissue with a high amount of fat, like brain and nervous tissue, encapsulating them in non-hydrophobic containers will allow them to circulate for longer in the blood stream, and giving them a higher probability of reaching the target location. Many chemotherapeutic drugs are strongly hydrophobic, so this possibility holds great potential in cancer treatment [2].

Extravasation To reach the tumor cells, the NPs need to exit the vasculature at the right location. Healthy blood vessels are highly organized and the endothelial cells lining these vessels are lined up side-to-side without gaps in between. Generally, NPs are too large to escape these vessels, and the probability for extravasation here is low. As mentioned before, tumor vasculature is less organized, more heterogeneous and typically show gaps between the endothelial cells [18], allowing NPs to exit. This phenomenon is the basis of passive targeting to tumors using NPs, and will be more thoroughly discussed in Section 2.2.2.

NP extravasation can happen either by diffusion or convective extravasation. The latter is possible in the tumor periphery, but diffusion is the main method of escape in the centre of the tumor. This is because of increased interstitial pressure here, a fact that will be discussed in Section 2.2.2.

Transport through extracellular matrix The ECM can be described as the component of the tissue that is not cells. It exists in all tissues including tumor tissue. A variety of molecules make up the ECM, including a hydrogel

built up of proteoglycans, and different structural components like collagen, elastin and fibronectin [28].

For a tumor to be completely eradicated, all the cells of the tumor needs to receive the chemotherapeutic drug delivered by the NPs. To reach the individual cells, the NPs need to travel through the ECM. In this process, the size of the NPs can pose a challenge for two different reasons. First, the high IFP in tumors ensure that the NPs can only move through the ECM by diffusion. The speed of which they do so is limited by their size, according to Fick's first law, Equation 2.1, meaning larger NPs will move more slowly than smaller ones. Second, the tumor ECM is especially crowded, with a large density of cells, collagen fibers and other ECM components. These components all pose a significant steric hindrance to diffusion, and smaller particles will have a easier job navigating the crowded environment of the tumor ECM than larger particles. This challenge can be alleviated by using smaller NPs, but this is always at the expense of drug payload. The size of the NPs to be used is therefore a matter that needs to be decided with several factors in mind.

$$J = -D\frac{d\varphi}{dx} \tag{2.1}$$

; where J is the flux, $\frac{d\varphi}{dx}$ is the concentration gradient with respect to space and D is the diffusion coefficient given for small spheres in a three dimensional fluid by Equation 2.2:

$$D = \frac{T}{6\pi\eta a} \tag{2.2}$$

; where T is the temperature, η is the viscosity of the fluid and a is the radius of the sphere.

Cellular uptake Most drugs, including chemotherapeutics, need to enter the cell to have an effect [2]. For NPs delivering drugs, several possible methods of achieving this are available. First, particles can release the drugs outside the cellular membrane, which the drug then penetrates alone. Second, the delivery can be contact mediated or happen by membrane fusion of the delivery vessel and the cell [29]. Finally, the entire NP can be taken up by the cell. In the latter case, the size of the NP ensures that the uptake is most likely to happen by endocytosis, where the cell uses a portion of the cell membrane to form a vesicle for the particles [30].

For the drug to reach the desired intracellular compartment, which in the case of most chemotherapeutics is the nucleus [2], the drug or the container needs to be able to withstand lysosomal degradation. Their natural purpose being to digest different biological components, lysosomes have a low internal pH and a high content of enzymes [31]. This needs to be considered when manufacturing NPs for drug delivery.

2.2.2 The enhanced permeability and retention effect

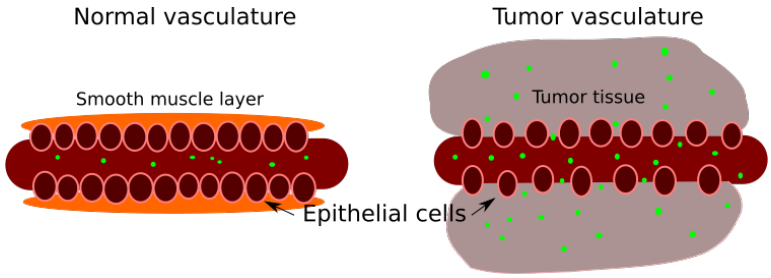

Figure 2.3: Illustration of the EPR effect. Left: healthy vasculature displays tight junctions between endothelial cells, and an intact layer of smooth muscle surrounding the vessels. NPs do not escape into the tissue. Right: tumor vasculature is leaky, with large openings between endothelial cells. NPs can escape into tumor tissue. Illustration by the author.

Tumors are dense, and tumor cells have increased proliferation compared to healthy cells. The increased activity and increased amount of cells naturally leads to an increased need for oxygen and nutrients [18]. To receive more oxygen and nutrients as the tumor grows, the tumor cells must constantly signal for more blood vessels. Due to the fast-growing nature of tumors, the endothelial linings of the vessels are not able to close properly and the vessel walls become leaky [7].

In healthy tissue, waste products and excess fluids are removed via the lymphatic network, which provides drainage of tissue. Due to their fast-growing nature, tumors lack a sufficient lymphatic network [27, 32]. This deficiency leads to a build up of IFP inside the tumor.

Together, the leaky vessel walls and elevated IFP of tumors comprise the EPR effect of macromolecules in solid tumors, first described by Matsumura and Maeda in 1986 [6]. Due to leaky blood vessels, larger molecules or particles are able to extravasate into tumor tissue to a higher degree than what would be possible for healthy tissue. Due to insufficient lymphatic drainage, macromolecules or particles remain in the tumor tissue for a longer time than they would in healthy tissue. The EPR effect is illustrated in Figure 2.3. The effect is only valid for macromolecules and particles, and does not apply to smaller molecules, for instance free chemotherapeutic drugs. This is because their small size will ensure rapid diffusion back into the blood stream and renal clearance [32].

The EPR effect seems like the perfect basis for a passively targeted DDS delivering drugs to tumors. There are however, several unresolved issues that needs to be addressed before DDS based on the effect can become a clinical success. The main problem concerning the EPR effect is its heterogeneity across tumors, between different tumor types, between individual tumors of the same type, and within single tumors. This arises from several factors: the degree of angiogenesis can differ between tumors, as can its degree of lymphatic drainage. Other biological factors that contribute to the heterogeneity of the EPR effect are the density

of the tumor growth adjacent to vasculature, perivascular growth, and the density of connective tissue in this space [25].

All these differences between or across tumors have their impact on the EPR effect. For example, the EPR effect may be more effective in well perfused parts of the tumor. Blood vessels surrounded by a dense network of cells or connective tissue are likely to experience less extravasation of macromolecules. In addition, high IFP or SS in tumors can cause collapse of blood vessels, rendering them non functional.

In addition to the issues explained above, the EPR effect is inherently self-attenuating because the increased flow of components from the blood *into* the tumor, and the decreased drainage of waste products *out of* the tumor, creates a high interstitial pressure in the tumor [25, 27]. This will to some degree negate the further inflow of macromolecules from the blood vessels, especially in the centre of the tumor where the IFP is typically higher.

In summary, several significant barriers must be overcome by NPs in order to reach the tumor cells and release their therapeutic payload. The inability to overcome some or all of these barriers is one of the reasons why NP DDSs have not yet seen much clinical success. Different strategies to enhance the possibility of NPs to overcome the barriers have been explored. In this thesis, US was used to help overcome the barrier of extravasation and ECM penetration.

2.3 Ultrasound

Sound is the transport of energy through molecular vibrations from a transmitter to a receiver. The motion of the molecules is termed compression when they are pushed closer together and rarefaction when they are separated. It is this mechanical motion of the molecules that create sound. Therefore, a sound wave is a mechanical wave [33].

The frequency with which the molecules in a sound wave vibrate determines the pitch of the sound. In a well known situation, the transmitter of the sound is a human voice, and the receiver is a human ear. However, the human ear can only register a limited range of sound frequencies, from about 20 Hz to 20 kHz. Sound waves with a frequency above 20 kHz are what is called ultrasound (US). In the following sections, the use of US in medicine, both for diagnostic and therapeutic purposes, will be discussed, and an explanation of the most important physical parameters of US will be given.

In medical applications, diagnostic or therapeutic, the US signal is generated by a transducer. To generate an US signal, an electric signal is translated to a linear motion by a piezoelectric crystal. The result of this motion of the transducer is a series of pressure waves, or sound waves, on the surrounding medium. The electric signal determines the frequency with which the transducer moves, and thereby the frequency of the sound wave.

All acoustic waves are either longitudinal waves, or shear waves. Their classification depends on whether the particles in the medium in which the wave travels move in the same direction as the wave (longitudinal waves), or in a direction which

is perpendicular to the wave (shear waves). The two forms of acoustic waves are illustrated in Figure 2.4. While longitudinal waves can travel in any medium, only solid media experience shear waves. Most biological tissues are soft and resemble a liquid more than a solid, and therefore only experience longitudinal waves. The exception is bone, which is a solid tissue. Shear waves can therefore arise in bones.

Just like other waves, US waves are described by certain wave parameters, like Amplitude (A), wavelength (λ), frequency (f) and period (T). The amplitude of an US wave is the difference between the peak compressional value and the peak rarefactional value of the wave. The wavelength is the distance in space between two identical points on the wave. The frequency is the number of wave cycles per second, and the period is the time it takes for one wave cycle to occur. The relationship between the velocity (c), wavelength, frequency and period of a wave is given in Equation 2.3.

$$c = \lambda f = \frac{\lambda}{T} \tag{2.3}$$

The velocity is dependent of properties of the medium in which it travels according to Equation 2.4.

$$c = \frac{K}{\rho}^{0.5} \tag{2.4}$$

;where K is the elasticity and ρ is the density of the medium.

The generation mode of an US wave is a classification of the temporal characteristics of the waveform. There are two main generation modes: continuous wave (CW) mode, where the transducer is continually excited with an electrical signal to create a continuous waveform, or pulsed wave (PW) mode, where the transducer is excited for short periods of time with longer pauses in between. The duration of the pulse in PW mode is described by the number cycles per pulse (N), and the period or frequency as shown in Equation 2.5.

$$\tau = NT = \frac{N}{f} \tag{2.5}$$

The fractional amount of time in which the US transducer is activated in PW mode, is given by the duty fraction (DF) as in Equation 2.6.

$$DF = \frac{\tau}{PRP} = \tau PRF \tag{2.6}$$

;Here, the pulse repetition period (PRP) is the amount of time from the start of one pulse to the start of the next, and the pulse repetition fraction (PRF) is the number of pulses per time unit.

Ultrasound imaging, which will be discussed in Section 2.3.1, is based on the impedance (Z) of the media which the US beam travels through. The impedance differs between media and is given in Equation 2.7.

$$Z = \rho \times c \tag{2.7}$$

When the US wave passes an interface between two media, it is split into two new waves: one is reflected back, and the other continues into the new medium, it is refracted. The fraction of the wave which is reflected depends on the impedance of the two media as shown in Equation 2.8

$$R = (\frac{Z_1 - Z_2}{Z_1 + Z_2})^2, \tag{2.8}$$

where Z_1 is the impedance of the medium which the beam comes from, and Z_2 is the impedance of the medium which the beam continues into.

A final parameter which is relevant for the uses of US described in this thesis, is the mechanical index (MI), given by Equation 2.9. The MI is a measure of the non-thermal effects of US on biological tissue, a topic which will be thoroughly discussed in Section 2.3.2.

$$MI = \frac{P_{neg}}{\sqrt{f}} \tag{2.9}$$

;Where P_{neg} is the peak negative pressure [MPa] and f is the frequency [MHz] of the US.

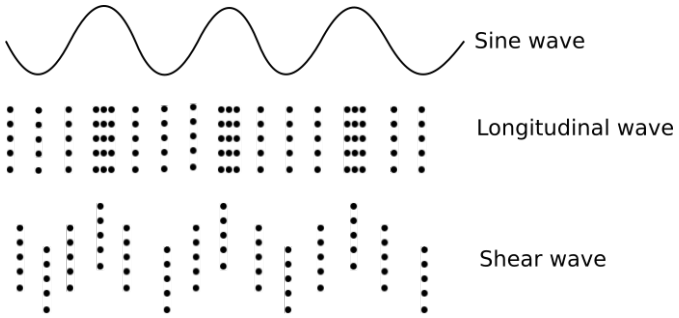

Figure 2.4: Illustration of longitudinal and shear waves. In longitudinal waves, the particles in the medium which the wave travels through move in the same direction as the wave propagation. In shear waves, the particles move in the directional which is perpendicular to the wave propagation. Illustration by the author.

2.3.1 Diagnostic ultrasound

US is widely used for clinical imaging and for imaging in research. US imaging is virtually risk- and pain free for the patient, and the equipment is accessible and easy to handle. In addition, US waves have a greater ability to penetrate tissue than visual light in most cases, and images can therefore be obtained for structures that are not easy to reach via other means [34]. In this section, the principles behind US imaging will be explained, and some important features of US images will be discussed.

To create an US image, US waves are emitted from a transducer. In most cases, there is actually an array of transducers positioned together to form an US probe. Each of these transducers are activated by electrical signals, and parallel US waves are generated. The medium in which these waves travels, will impact the waves in a manner that is exploited in US imaging. When a US wave encounters a boundary between two media with different acoustic properties, or impedances, a fraction of the wave will be reflected, as given in Equation 2.8. This fraction will subsequently be detected by the transducer. The portion of the wave that did not get reflected will continue through the boundary, until it encounters a new boundary which will reflect a new portion and so on. The US image is created from a calculation of the distance between each tissue boundary, which can be obtained from the time from generation of the original signal to the reception of the reflected signal, and the velocity of the US in the tissue [35]. For most biological tissues, the velocity of the US wave is approximated to 1540 m/s [36].

To increase the contrast in US images, US contrast agents like gas MBs are used. The difference in acoustic impedance between the gas bubbles and the surrounding medium increases the contrast in the image. When injected into blood vessels, MBs provide a method for visualizing the blood vessel network. MBs are usually in the size range of $1 - 10\,\mu m$, ensuring that if administered intravenously, they will resist extravasation [37].

An US image is created from data that lies in the US beam path, and is therefore not oriented in the same way as images made from light. One direction in the image is the same as the beam path direction, and the other direction is perpendicular to the beam path direction. The directionality of US images is illustrated in Figure 2.5.

Resolution is an important concept in all imaging. The resolution is the smallest distance that two objects can be separated by, and still be discerned as two individual objects. In two dimensional US imaging, the concept of resolution is divided in two directions, namely axial and lateral resolution. The axial resolution is the resolution in the direction of the US beam axis. The axial resolution is related to the spatial distance occupied by the US wave in the medium, which equals the wavelength. In PW mode US, the spatial pulse length (SPL) is the spatial distance occupied by one pulse of the US beam, given by Equation 2.10. The best axial resolution available equals $\frac{SPL}{2}$ [36].

$$SPL = N\lambda = \frac{\tau\lambda}{T} = \tau f\lambda \tag{2.10}$$

The lateral resolution of an US image is the resolution in the direction perpendicular to the US beam. The best lateral resolution available equals the minimum beam width of each US beam [36].

As shown in Equation 2.10, the axial resolution of an US image is dependent of the frequency of the US wave. A higher frequency will result in better resolution. However, increasing the frequency of the US wave will also increase attenuation of the wave in with a factor of approximately 0.7 dB/cm MHz [36]. The increased attenuation of the wave leads to a shorter penetration depth, which in Figure 2.5 is the vertical extent of the US image.

In addition to scattering of the US beam due to differences in impedance between different media, the US beam is attenuated by heat dissipation. This is the process where some of the energy from the US wave is absorbed into the tissue as heat. If the rate of heat production is greater than the rate of heat removal, this will result in a temperature increase in the tissue [36]. While this is normally undesired in diagnostic US, it is sometimes exploited in therapeutic US, as described in Section 2.3.2.

No image is an exact representation of the real world, but contains image artifacts. This is also the case for US images, which have a specific set of artifact types. When analyzing US images, it is important to be aware of these artifacts to avoid misinterpreting the images. Below follows a short description of some common artifacts that are relevant to the type of US images analyzed in this project [33].

Noise appear in many image types including US images, and can be observed as irregularly spaced, small, bright specks in the image. Noise is caused by fluctuations in the imaging electronics and can often be removed relatively easily by image processing software.

Reverberations arise from multiple reflective interfaces that reflect the US beam between each other. They appear as a series of parallel lines and can interfere with actual structures in the tissues.

Ring down artifacts arise from fluids trapped between tetrahedrons of gas bubbles and appear as a continuous signal. Like reverberations, ring down artifacts can interfere with structures or their boundaries in the image.

Mirror image artifacts appear behind structures with strong reflectory abilities as a mirror image of the structure.

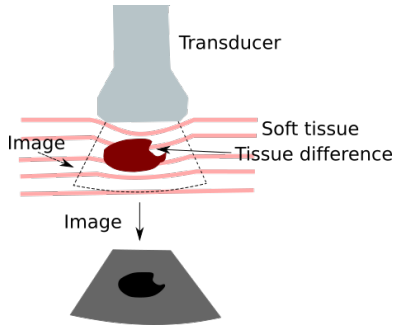

Figure 2.5: Illustration of the directionality of US imaging. The resulting image is from the plane perpendicular to the face of the transducer. Illustration by the author.

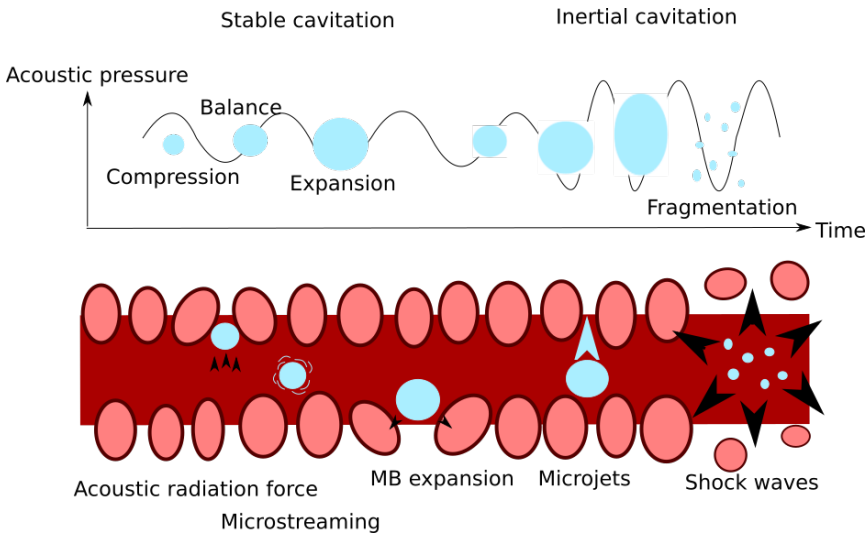

Figure 2.6: Stable and inertial cavitation of MBs. Top: The effect of ultrasound on MBs. MBs are compressed at high acoustic pressure and expanded at low acoustic pressure. Increase of the amplitude of the acoustic pressure beyond a certain limit will result in MB implosion and fragmentation. Bottom: Non-thermal effects of therapeutic US combined with MBs. From left: acoustic radiation force (caused by US alone), microstreaming and MB expansion (caused by stable and/or inertial cavitation), and microjets and shock waves (caused by inertial cavitation). Illustration by the author.

2.3.2 Ultrasound in nanoparticle drug delivery

While US waves have an important role in diagnostic imaging, they also have great potential as part of therapeutic systems. Ablation of kidney stones and moderate tissue heating in physical therapy are some applications of therapeutic US today [34]. In this thesis, a DDS using US combined with US contrast agent MBs to increase delivery of NPs carrying chemotherapeutics to solid tumors will be characterized. It is therefore necessary to explain the known effects of US waves on MB and NPs.

The exploitation of the EPR effect has been the most promising method of passive targeting regarding NP drug delivery for the last decades, but it has not yet proven to be reliable enough for the strict demands of clinical medicine [22, 25]. In the project behind this thesis, an active form of targeting with the intention of enhancing the EPR effect has been studied.

The DDS described here was based on PEGylated Poly(2-ethyl-butyl cyanoacrylat) NPs used as a stabilizing shell around MBs. The NPs carried fluorescent model drugs, in order to be examined in with fluorescent microscopy. The NPMBs were injected intravenously, and US was applied externally at the tumor location. It is the interaction between the US waves and the MBs that enhances the already

existing EPR effect.

In this project, as in several other in recent years [34, 8, 9], US and MBs were used in a therapeutic purpose, rather than a diagnostic one. While diagnostic US has a low energy deposit to the tissue it is applied to, the opposite is true for therapeutic US: it is the deposition of energy that produces the desired effects. These effects can largely be divided into thermal and non-thermal effects, and are described below:

Thermal effects Hyperthermia, or heating of the tissue, occurs when the tissue absorbs acoustic energy. This phenomenon has proven to cause several effects that can be exploited in drug delivery. The most important of these are the increased blood flow and the increase in vascular permeability caused by the elevated temperature [9]. The increased blood flow to the heated area will lead to a higher influx of blood carried therapeutic agents here. The increased vascular permeability will allow a higher share of the agents to escape the blood vessels.

It is also possible to design a DDS to release the therapeutics in response to elevated temperatures, by using temperature-sensitive nanocarriers [8].

Non-thermal effects The non-thermal effects of therapeutic US are illustrated in Figure 2.6.

The direct force of the US beam on the medium it is applied to, is termed acoustic radiation force (ARF). This transfer of momentum in the direction of the applied beam will cause a bulk movement of the medium in question called acoustic streaming. ARF has been shown to cause movement of objects, including NPs [38] and MBs [9] in the blood stream. In addition, ARF has been shown to be able to disrupt the ECM and thereby increase the efficiency of interstitial transport [9].

Due to the size of the MBs being smaller than the wavelength of the acoustic waves of US, the MBs will respond to the radiation by oscillating according to the pressure cycle of the US [8]. When the pressure is high, the bubbles will contract, and likewise they will expand when the pressure is low. This phenomenon is referred to as cavitation. A widely used classification of the cavitation behaviour of MBs is the MI as given in Equation 2.9.

Cavitation can occur spontaneously without the presence of MBs, but the MBs will act as cavitation nuclei if present, and in this case the cavitation will occur at a lower MI [8]. The occurrence of cavitation is greater in the blood stream than in interstitial space, due to the available space in which the bubbles can oscillate [9].

Cavitation can be stable, in which case the MBs keep oscillating around an equilibrium radius. As opposed to stable cavitation, inertial cavitation occurs when the MI is so high the amplitude of oscillation keeps increasing, until it causes the bubble to implode [8]. The US intensity needed to induce inertial cavitation depends on the size of the bubble, and the thickness and stiffness

of the shell surrounding it, as well as the pulse duration and repetition rate of the US [39] in addition to the MI.

During both stable and inertial cavitation, the oscillating bubbles create displacement of the fluid surrounding them, known as microstreaming [40]. This in turn leads to shear forces on the capillary walls, and has the potential to increase the vascular permeability and thereby increase the extravasation [10]. The velocity of these microstreams is proportional to the amplitude of the oscillation [40].

The collapse of the MB under inertial cavitation produces still more potent effects than those of the stable oscillation. In addition to elevation of temperature, emission of light and creation of free radicals [8], more useful effects like shear forces, shock waves and jet streams are produced. These have the potential to produce pores in the vascular wall where NPs can extravasate [9]. If the implosion of the bubble happens near the blood vessel wall, or else near a cellular membrane, it has been shown to have a greater potential to disrupt these by creating microjets [8]. Furthermore, it has been suggested that the force created from inertial cavitation has the potential to cause capillary rupture [34].

Together, the thermal and non-thermal effects of combining MBs and US are promising in enhancing the EPR effect of therapeutic NPs by forcing the particles out of the blood stream and into the tumor if the US is applied to the right location. The possible disruption of the tumor ECM is another reason why this approach can help the NPs overcome the barriers to reaching their target location. The DDS characterized in this thesis has already shown highly promising results by bringing breast cancer xenografts in mice into complete remission [11].

2.4 Fluorescence imaging

Fluorescence microscopy is one of the most important characterization techniques in cell biology research, and it is the main technique used to characterize the DDS in this project. The excellent contrast provided by this technique, along with the many possibilities for different advanced methods of imaging, makes fluorescence microscopy unique in its ability to image cellular structures and functions. This section will include a short explanation of the main principles behind the technique, as well as some common pitfalls that are associated with fluorescence microscopy.

In fluorescence microscopy, the image contrast is provided by the light from one or several fluorescent molecules, or fluorophores. A fluorophore is a molecule that is optically excited by light from a specific wavelength range, and that emits light of another specific, longer, wavelength range, upon deexcitation [41]. This principle is illustrated in Figure 2.7.

Fluorescence can be provided by either autofluorescent structures, like collagen, or fluorescent probes. Fluorescent probes are used to stain specific structures of a sample by selective bonding. There are a large number of different probes commercially available [42], suitable for staining a range of different structures.

A fluorescent microscope is set up to focus light of the excitation wavelength onto the sample and collect the emitted light from the fluorophores. The most important components for this purpose are listed below and illustrated in Figure 2.8 [41]:

- Excitation light source: most commonly a mercury arc lamp or a laser.
- Excitation filter: a filter that only lets the desired wavelength of exciting light pass. The filter is changed according to the fluorophore in use.
- Emission filter: Used to separate the relatively weak emitted light from the relatively strong excitation light.
- Lenses and dichroic mirrors: collector, condenser and objective lenses are placed at specific places to focus the light from one specific location in the light path to another. An important feature of the lenses is their numerical aperture (NA), representing the range of angles over which they can accept or emit radiation. Dichroic mirrors allow certain wavelength to pass, while reflecting others. They are used to direct the light path in the microscope.
- Photodetectors: used to digitally record the image formed from the emitted light, photodetectors can for example be CCD cameras. In CLSMs, described in Section 2.4.1, the photodetector is usually a photomultiplier tube (PMT), which detects light from a single point and multiplies it.

A few concepts are important to be aware of when working with biological specimens and fluorescence microscopy. The most relevant ones are described below.

Bleedthrough Is the phenomenon of detecting fluorescence from a neighboring channel in the channel of interest, i.e. more than one fluorophore is detected when there is only supposed to be one. This naturally causes problems for subsequent image analysis. This issue can be addressed by choosing the most suitable filter for each fluorophore, or even choosing fluorophores with properly separated emission spectra.

Photobleaching Refers to the phenomenon where a fluorescent molecule is permanently photochemically destroyed, usually by oxidation [41]. This is apparent by the gradual loss of intensity of the emitted light of the fluorophore, and will eventually happen to all fluorophores that are exposed to excitation light. Some fluorophores however, are more photostable, which means they can withstand a larger amount of light before photobleaching. To reduce the extent of this issue, measures like reduction of laser intensities, addition of reactive oxygen scavengers and reduction of imaging time can be considered.

Phototoxicity In addition to the thermal effect of radiating a biological sample with electromagnetic radiation and the possible secondary effects arising from that, the light itself has potential photochemical effects on cells and/or tissue. Denaturation of proteins and loss of enzymatic activity in living cells are examples of possible consequences, as are chemical alterations of molecules in the specimen [43].

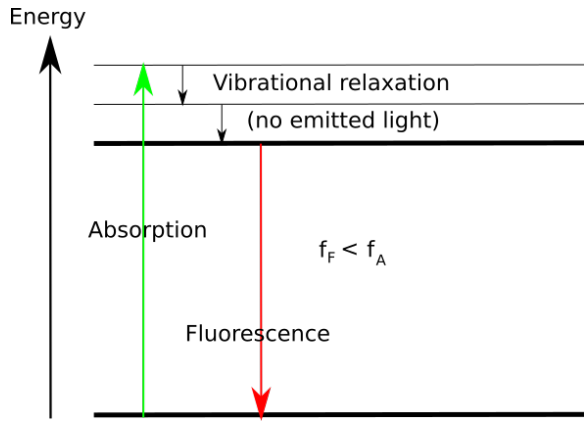

Figure 2.7: Illustration of a Jablonski diagram showing the different states of a fluorophore. The incoming light excites the fluorophore from the ground state. The fluorophore loses energy through non-radiative transitions between vibrational states to reach the excited state. Thus the fluorescence emitted has a longer wavelength than the exciting light. Illustration by the author.

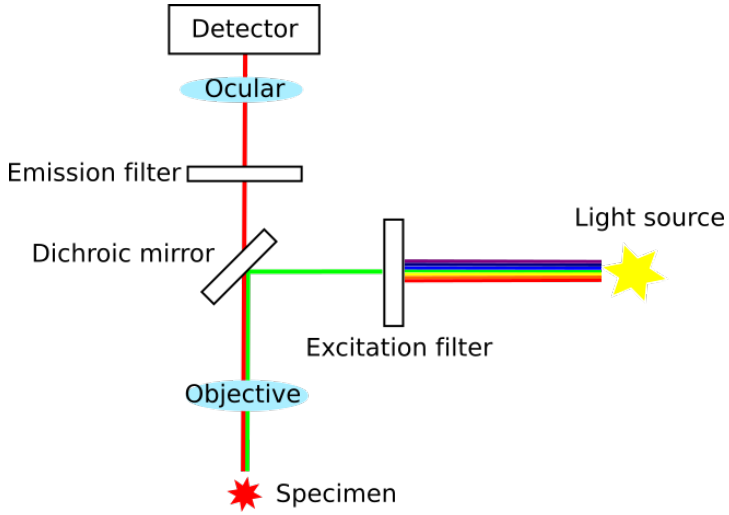

Figure 2.8: Schematic of the setup of a fluorescence microscope. Light from the light source hits the excitation filter and only the exciting wavelength passes. The light is then reflected by a dicrhoic mirror and focused by the objective to hit the sample. The sample is excited and emits fluorescent light of a shorter wavelength, which is focused by the objective and allowed to pass through the dichroic mirror. The emission filter filters any unwanted wavelengths, and the ocular focuses the emitted light onto the detector. Illustration by the author.

2.4.1 Confocal laser scanning microscopy

In widefield microscopy, the entire sample is illuminated at once, and in the same way, the emitted light from the entire sample is collected. When doing this, the resulting image becomes the sum of the images throughout the sample depth, both those in the focal plane and those outside. If the distance between the upper and lower region of the focus region, i.e the depth of field (DOF), is large, this is not a significant problem. However, for samples imaged at high magnification, a high NA lens with a low DOF is required, and the out-of focus light becomes a problem [43].

In confocal fluorescence microscopy, only the focused emission light from a small, diffraction limited, region of the sample is collected. To achieve this, a pinhole aperture is placed in the image plane of the sample. The position of the pinhole determines which light reaches the detector, and light that is out of focus will be filtered out, as it does not converge on the pinhole. The use of a laser excitation source ensures that the excitation light is also focused to the same small region[44]. The principle of a confocal aperture is illustrated in Figure 2.9.

Using a pinhole aperture requires a stronger excitation light intensity to achieve the desired amount of fluorescence, as a proportion of the signal is blocked by the aperture. Therefore, the issues related to strong excitation light sources, like photobleaching or phototoxicity, should always be kept in mind when using a confocal microscope.

To obtain a full image, the imaged spot must be scanned across the sample. A microscope that uses this technique and scans the focused emission-collection spot across the sample is called a CLSM. The scanning is done either for the exciting laser beam, or the stage on which the sample sits. Although moving the laser can cause aberrations by the lenses, it is most often preferred to scanning the sample stage when examining biological samples, simply because moving the specimen can cause disturbances in the soft tissue than can distort images [43].

The use of a pinhole creates an "optical section" within the sample, which can be moved up and down by moving the sample stage. The size of the pinhole determines the depth of the optical section. This is measured in Airy units (AU), where a larger AU indicates a more open pinhole, and therefore a thicker optical section. The possibility to create an optical section that can be tailored in depth and can be moved in z-direction, makes it possible to create 3D images using a CLSM. When doing this, the scans from each optical section are saved and a 3D-image is reconstructed by appropriate software.

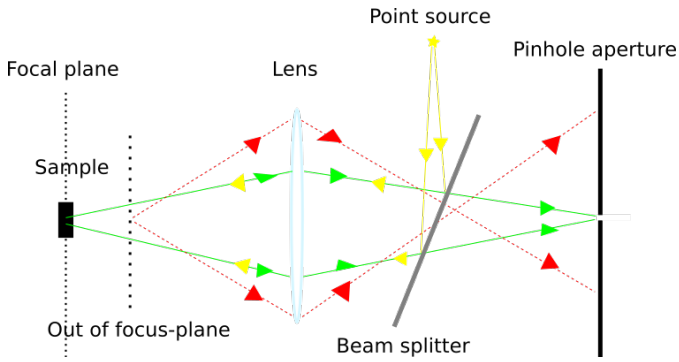

Figure 2.9: Schematic of the beam path from point source to sample, and from sample to confocal aperture (pinhole) in a confocal laser scanning microscope. The confocal aperture allows only in-focus light to reach the detector. Illustration by the author.

2.5 White light interferometry

White light interferometry (WLI) uses white light to to map the surface of a three dimensional sample. The technique can be used to detect height differences in the range of approximately 10 nm to a few cm. WLI is a non-contact method and does therefore not involve damage of the measured surface [45].

In WLI, constructive and destructive interference between waves that are either in phase or out of phase, is used to collect topographic data, by calculating the distance from the source to the sample at different coordinates. The technique is not new, but has been made more powerful and easy to use by modern electronics and data analysis techniques [45].

Chapter 3

Methods

3.1 Cell culture

Human prostatic adenocarcinoma (PC3) cells (American Type Culture Collection) and human osteosarcoma (OHS) cells (Department of tumor biology, the Radium Hospital, Oslo [46]) were cultured with the aim of implantation into animals. PC3 cells were cultured in Dulbecco's Modified Eagle Medium (DMEM, Gibco by Life Technologies) with 10 % fetal bovine serum (FBS) (Sigma Aldrich) and 1 % Penicillin Strepotimycin. OHS cells were cultured in Roswell Park Memorial Institute (RPMI) 1640 Medium (Thermo Fischer) with 10 % FBS (Sigma Aldrich) and 1 % Penicillin Strepotimycin.

All cells were grown first in 75 cm^2 flasks (VWR) containing 15 ml growth medium, then transferred to 300 cm^2 flasks (VWR) containing 60 ml growth medium in order to grow enough cells for implantation. All cells were incubated at 37°C with 5 % CO_2. Medium change was performed twice per week, and cells were split once per week during the culturing period.

A description of the cell splitting process from 300 cm^2 (75 cm^2) flasks follows. Cell splitting was performed by removing the growth medium from the flask, before adding 20 ml (5 ml) phosphate buffered saline (PBS, Sigma Aldrich) to wash the cells. To detach the cells from the flask surface, the PBS was removed and replaced with 12 ml (3 ml) 0.25 %/0.02 % Trypsin/EDTA (Sigma Aldrich) and the flask was placed at 37°C for approximately 3 min. Detachment of the cells was confirmed using a light microscope (Leica DMIL). Next, 28 ml (7 ml) growth medium was added to the flask and carefully pipetted to ensure detachment of all cells. One droplet of the suspension was transferred to a Bürker chamber to be counted under a light microscope. The remaining suspension was then transferred to a 50 ml (14 ml) centrifuge tube (Corning Centristar) and centrifuged for 5 min at 1500 RPM (Heraeus Instruments, Megafuge 1.0). The supernatant was removed, and growth medium was added to the centrifuge tube to make a cell concentration of 1×10^6/ml, according to the previous counting. The growth medium was pipetted back and forth to make an even suspension of cells. Finally, 6 ml (1.5 ml) suspension,

containing 6×10^6 (1.5×10^6) cells, was transferred to a new flask, and the flask was filled with growth medium to make the final content 60 ml (15 ml).

When harvesting cells for implantation, the procedure for splitting of cells was followed up to and including centrifuging the cells at 1500 RPM for 5 min. After removing the supernatant, 4 ml growth medium was added to the centrifuge tube, and pipetted to dissolve the cell pellet into a new suspension. Cell suspensions from different centrifuge tubes were then transferred together to a 14 ml centrifuge tube and centrifuged at 1500 RPM for 5 min. After removal of the supernatant, cell medium was added to make a cell concentration of 3×10^6 cells/µl. The medium was pipetted to dissolve the pellet and make an even cell suspension. The cell suspension was transferred to 2 ml tubes (VWR) and kept on ice until implantation.

3.2 Animal trials

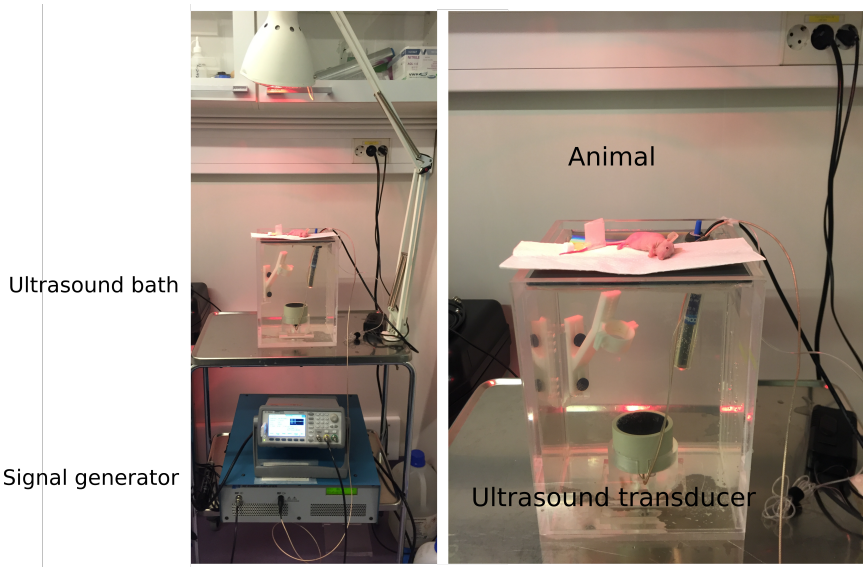

Figure 3.1: Image of the treatment setup for animals in the treated groups. Left: setup with the signal generator, US bath and heat lamp. Right: Close up of the US bath with US transducer and the animal lying on its side with its hind leg submersed in the bath.

All experimental procedures involving animals were in accordance with the Norwegian Animal Research Authorities. Animals were kept in pathogen free conditions in individually ventilated cages (22-23°C, 50-60 % relative humidity) containing 4 animals each. The animals had free access to food and sterile water at all times. Whenever the animals were under anaesthesia, their body temperature was kept stable by external heating, and eyes were kept moist using Viscotears Liquid

gel (Alcon). All animals were euthanized while under anaesthesia, using cervical dislocation.

Tumors from three different animal trials, executed summer 2017 and spring 2018, were used in the experiments described in this thesis. All trials were performed by Einar Sulheim. The author assisted in the second and third trial, but did not handle the animals. The three trials were aimed to be as similar as possible, and unless otherwise stated, any description in the next section can be assumed to be the case for all trials.

3.2.1 Animals and treatment

Prior to tumor implantation, athymic Balb/c nude mice were anesthetized using Isoflurane and marked for subsequent identification with ear clippings. Tumors were implanted subcutaneous on the left hind leg of the animals. Tumors used were either Prostate carcinoma PC3 or Osteosarcoma OHS, cultured as described in Section 3.1.

In Trial 1 and Trial 3, the treatment was given when tumors reached a size of approximately 10 mm in the longest axis. In Trial 2, the treatment was given approximately three weeks after tumor implantation. Trial 3 was performed because the PC3 tumors from Trial 2 turned out smaller than OHS tumors, making it impossible to eliminate size related explanations behind differences between the two groups.

Before treatment, the animals were randomly distributed into the groups as shown in Table 3.1 and anesthetized by a subcutaneous injection of fentanyl, medetomidine, midazolam and water (2:1:2:5) at a dose of 0.1 mL per 10 g.

All animals were given a slow bolus (injection lasting for 10-15 seconds) of 100 µL NPMBs (SINTEF) with NPMB concentration of 10 mg/mL. The animals in the treated groups were treated with US for 2 min. The US treatment was initiated at injection start. The tumors in the treated groups received 10,000 cycles of 1 µs US bursts every 100 ms ([PRF]= 10 Hz) repeated for 0.5 s, followed by a break lasting 1.5 s ([Global PRF]=0.5 Hz, total duty cycle 2.5 %). The US had an MI of 0.5, and total destruction of MBs was expected.

The US treatment was the same as the one originally used by Snipstad et al. [11]. A custom made, single-element focused transducer with a center frequency of 1 MHz (Imasonic, Besancon, France) was used. Signal generation was done by a waveform generator (33500 B, Agilent Technologies), and amplification by a 50-dB power amplifier (2100 L, EI, Rochester, NY, USA). As illustrated in Figure 3.1, the transducer was mounted at the bottom of a water bath. The animal was placed on top of an absorber coated lid covering the US bath, with its tumor bearing leg submersed into the water through a 10 mm hole in the lid. To avoid hypothermia and reduced blood flow in the mouse, the water was heated to 34°C using an aquarium heater (Trixie aqua pro heater), and the animal was heated using a heat lamp above the setup. To cover the entire tumor by the US beam, a distance of 190 mm was kept between the transducer and the tumor.

All animals were imaged at various time points up to euthanization in a small animal optical imager (Pearl Triology). Prior to euthanization, a 100 µL injection of

LECTIN was given intravenously to stain vascular endothelial cells for subsequent imaging. The animals were euthanized after 6 h in Trial 1 and after 30 min in Trial 2 and Trial 3.

Tumors were removed from the animals immediately after euthanization. The tumors from Trial 1 were flash frozen in liquid N in Tissue Tec upon removal from the animal. In Trial 2 and Trial 3, the tumors were subjected to an experiment intended to measure the release of SS (see Section 3.4) before being frozen with the same method.

Sectioning of the tumors were performed by Ingunn Nervik at CMIC NTNU. In Trial 1, the tumors were sectioned into 25 µm sections from 3 different "depths" of the tumor. In trial 2 and 3, tumors were sectioned into 10 evenly distributed 25 µm sections starting from the cutting plane in the middle of the tumor, see planar cut method, Section 3.4

Table 3.1: Overview of groups for three different animal trials. The subsequent use of the images from each trial (HR CLSM images or SS measurements including tile scans of tumor sections) is specified. Treatment group, tumor type, and number of animals per group is given.

Trial 1: HR CLSM			Trial 2: SS measurements			Trial 3: SS measurements		
Group	Tumor	N	Group	Tumor	N	Group	Tumor	N
Treated	OHS	8	Treated	OHS	4	Treated	PC3	4
				PC3	3			
Control	OHS	8	Control	OHS	4	Control	PC3	4
				PC3	3			

3.2.2 Nanoparticle microbubble complexes

The NPs used in this project were PEBCA (poly (ethyl-butyl cyanoacrylate) NPs fabricated at SINTEF Trondheim [47]. The NPs had Z-average size of 177 nm, measured by dynamic light scattering (DLS). The particles has a PDI=0,17 and zetapotential of −2 mV.

All NPs were loaded with both NR668 (visible range dye) and DiR (near-IR dye), and surface coated with two different types of PEG: Kolliphor and Brij.

NPMBs were fabricated by mixing NPs (0.1 wt%) with 0,5% casein in PBS saturated with Perfluorpropane (PFP) for 2 min (UltraTurrax). The vial was closed with parafilm during mixing.

Figure 3.2 shows a scanning electron microscopy (SEM) image of the MB covered in NPs.

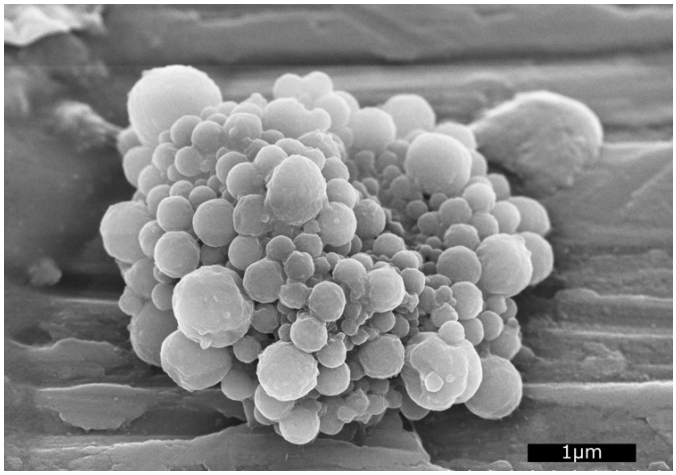

Figure 3.2: SEM image of a NPMB. Scale bar 1 µm.

3.3 Microdistribution of nanoparticles in OHS tumor tissue

3.3.1 Mounting of tumor sections

The tumor sections were kept frozen at −80°C between sectioning and imaging. Upon thawing, mounting medium (VECTASHIELD) with 4',6-diamidino-2-phenylindole (DAPI) fluorescent stain was added to the tumor sections, before placing a cover glass (VWR) on top and sealing with nail polish. In the Specialization project "Nanoparticle microdistribution in tumor tissue: a characterization of a drug delivery system based on microbubble cavitation" by the author, it was found that NPs and/or dye are mobilized in the mounting medium. The mobilization could be seen already 1.5 h after application of mounting medium. Therefore, the imaging was carried out within 1 h after mounting of the section, to prevent mobilization of the NPs and/or dye. All imaging was performed in room temperature.

3.3.2 High resolution CLSM Imaging

The tumor sections imaged in this part of the project were chosen from eight animals (Trial 1): four from the treated group and four from the control group. For each tumor, one tumor section from each of the three levels of the tumor was chosen for imaging. This resulted in a total of 119 images from the treated group and 117 images from the control group.

A 40x water objective with a NA of 1.1 was used for this part of the project. Each image was acquired in three channels: nuclei stained with DAPI, blood vessel endothelial cells stained with lectin-FITC and NPs stained with NR668. The chan-

nels were imaged in sequence (sequenced between frames) to prevent bleedthrough. All images were captured at speed 100 Hz, with a line average of 8. The imaging settings for this part of the project are presented in Table 3.2. The large optical section was in order to obtain a satisfactory signal to noise ratio of the images.

Images were chosen in a systematic manner based on visual identification of blood vessels in the ocular of the microscope. This was done by drawing up a sketch "map" of the tumor section before mounting, and marking each image location on the sketch during imaging, ensuring that blood vessels from the entire tumor section were imaged. In z-direction, a location was chosen so as to show a highest possible level of continuity of the blood vessels. Blood vessels within a certain distance, about 100 µm, from the edge of the section were avoided, due to an apparent accumulation of fluorescence in this area. In the imaging of PC3 tumor sections performed in the Specialization Project "Nanoparticle microdistribution in tumor tissue: a characterization of a drug delivery system based on microbubble cavitation" by the author (Section 4.1), image locations were chosen so that no blood vessels were present directly outside the image boundary. This was done to avoid recording false NP spreading from the vessels which were outside the field of view. However, due to the density of blood vessels in the OHS tumor sections, it was not possible to acquire the images in this manner.

Table 3.2: Imaging settings for imaging NP microdistribution in OHS tumor sections. Channel 1 imaged nuclei stained with DAPI, channel 2 imaged NPs stained with NR668 and channel 3 imaged vascular endothelial cells stained with lectin-FITC. The pinhole size of 3.59 gave an optical section of 4 µm. MP= multiphoton, WLL= white light laser.

Channel	1	2	3
Laser	MP	WLL	WLL
Wavelength	730 nm	561 nm	501 nm
Intensity	8%	21%	3%
Detector	HyD1	HyD3	HyD1
Detector range	400-450 nm	570-613 nm	510-560 nm
Detector gain	100%	150%	100%
Pinhole size	–	3.59 AU	3.59 AU

3.3.3 Image analysis

Images were analyzed in FIJI (Fiji Is Just ImageJ) [48]. Images were analyzed to acquire the mean and median distance of NPs from the nearest blood vessel wall. A detailed illustrated description of the procedure of this image analysis is given in Appendix A. For this analysis, both the blood vessel and the NP channel were used. Both channels were thresholded, i.e. all pixels with an intensity above a certain limit were assigned a new value of 255, and all pixels with a value below the same limit were assigned the new value 0, resulting in a binary image. This binary image would then consist of regions of interests (ROIs), by definition encompassing only

the fluorescent object (blood vessels or NPs, respectively). The threshold-value was chosen using the Triangle algorithm [49], included in FIJI. This particular algorithm was chosen after careful consideration and testing of several other algorithms, using a selection of images. The Triangle algorithm was chosen for both channels as it was the one that included most of the NPs or blood vessels without including noise.

In the blood vessel channel, a distance map was created from the binary image resulting from the thresholding. A distance map is an image where each pixel is assigned the value which is equal to the distance (in pixels) from that pixel to the nearest ROI. Thus, all pixels defined as blood vessels in the preceding thresholding were assigned the value 0, while other pixels were given a value representing their distance to the nearest blood vessel. The distance map is a built in feature in FIJI.

An ROI was created from the thresholded NP image and layered over the blood vessel image, thus marking on the distance map the location of the NPs. A histogram of the pixel values from the layover (equalling distance from NP to nearest blood vessel wall) was collected.

In addition to the distance from the nearest blood vessel wall, the amount of NPs inside/outside blood vessels was analyzed. This was done by comparing the amount of pixels defined as NPs with a distance 0 to the nearest blood vessel wall (NPs inside blood vessels) with the amount of pixels with a distance that differed from 0 (NPs outside blood vessels). The histogram values described above were used for this analysis.

Last, an analysis of the total accumulation of NPs in the tissue surrounding the chosen blood vessels was executed. This amount was represented by the amount of pixels defined as NPs in each image, acquired from the thresholded image from the NP channel (all pixels with value 255 after thresholding were defined as NPs). Note that this was not an accurate quantitative measure of the NP accumulation, but rather a method of comparing treated and control groups.

3.3.4 Artifact removal

In some images, clusters of NPs were observed some distance away from any blood vessels. It was suspected that such clusters were in fact NPs inside or directly outside un-stained blood vessels. To prevent these clusters from obscuring results, an algorithm was applied to the histogram data to remove them: if three histogram entries in succession were increasing, and the entry before those three was 0, the entire tail of the histogram would be given a value of 0. See an illustration of this artifact removal in Figure 3.3.

3.3.5 Statistical analysis

Data analysis for this part of the project was executed in Microsoft Excel. Data are presented as mean±standard deviation (SD). The data were assumed to approximate a normal distribution. Heteroscedastic student t-tests were used to determine significance of the results. Correlation coefficients were determined with Spearman's rank correlation tests as there were relatively many outliers were present.

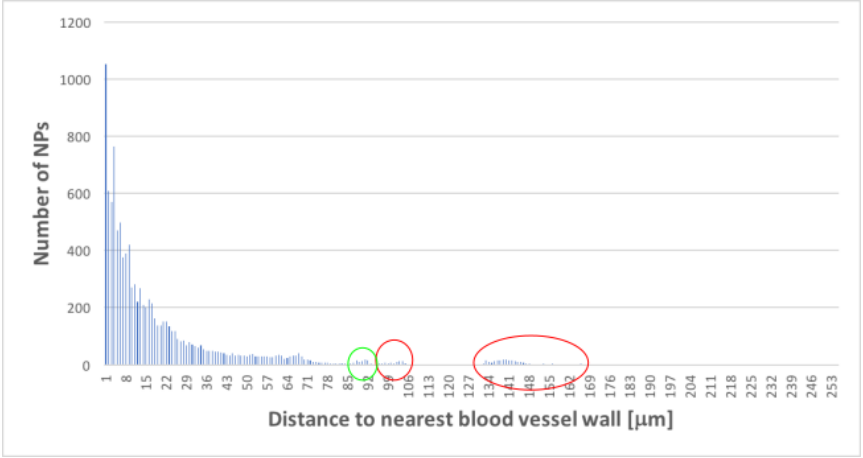

Figure 3.3: Illustration of artifact removal in image analysis. The histogram is an example of the histogram obtained per image during image analysis, showing the distribution of NPs according to their distance to the nearest blood vessel wall. The illustration shows three apparent clusters of NPs at a high distance from the blood vessels. The two clusters marked with red circles would be removed as artifacts, as they succeeded a bin containing 0 NPs. The cluster marked with a green circle would not be removed, as although it increases for three or more bins, the bin preceding the cluster does not have a value of 0.

3.4 Release of solid stress

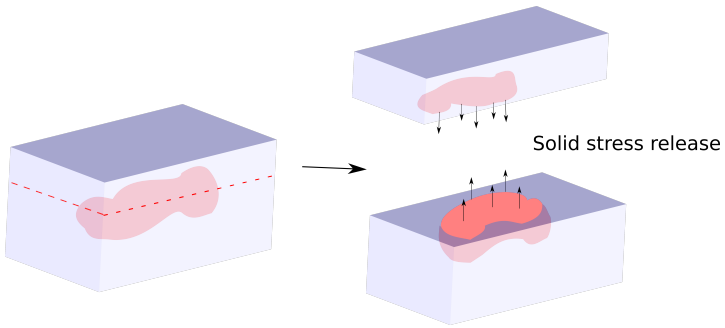

Figure 3.4: Illustration of the "Planar cut" method for releasing SS in tumors. The tumors were embedded in an agarose gel cast, which was cut horizontally in two after solidifying. The tumors had a tendency to sink towards the bottom of the gel cast before it was solidified, and it was practically difficult to cut the tumors in two equal parts. SS release within the tumor caused the cut surface to rise proportional to the level of SS.

3.4.1 Planar cut method for release of solid stress

The method used for releasing and measuring SS in tumors *ex vivo*, was the "Planar cut method", first described by Nia et al. [13].

Immediately after removal from the animal, each tumor was embedded in 2 % agarose gel made with PBS (Sigma Aldrich). Custom made casting molds made from aluminum foil were used to cast the gels. Tumors were submersed in gel solution at approximately 37°C, and the gel was solidified at room temperature. After embedding, the gels with the tumors were kept on ice until cutting.

The solidified gel with the tumor inside was removed from the casting molds prior to cutting. While still inside the agarose gel, each tumor was cut horizontally in two using a scalpel, to release SS along the cut surface, as illustrated in Figure 3.4. Because the tumors had a tendency to sink towards the bottom of the gel cast before it was solidified, it was practically difficult to cut the gel with the tumors in two equal parts. Both parts of the tumor were placed on a paper towel with the exposed cut surface facing up, to be imaged using US. The tumor halves were labeled according to a number corresponding to the animal of origin, and "A" or "B", one for each half of the tumor.

3.4.2 Optical profiling

An attempt was made to map the tumor halves by WLI using a Contour GT-K 3D optical profiler (Bruker). Several attempts were made: imaging the cut surfaces while the tumor was still embedded in the agarose gel cast, removing the tumor halves from the gel casts to image them, and coating the tumor halves in Pt to image them. The coating was performed with an AJA Sputter and Evaporator (AJA International Inc.). However, it was not possible to achieve sufficient interference from the sample in any of these forms, and the method could not be used.

3.4.3 Ultrasound imaging

Directly after cutting, the tumor halves were imaged using US. The tumor halves, still embedded in the agarose gel, were placed on a paper towel with the cut surface facing up. The friction between the paper towel and the moist agarose gel ensured that the samples did not move during the imaging process. Prior to imaging, the cut surface of the tumor halves was covered in Aquasonic 100 ultrasound transmission gel (Parker Laboratories).

The imaging was performed using a 400 MHz US transducer (VisualSonics). A 3D motor (VisualSonics) was used to move the sample between images, resulting in a stack of images and the possibility of recreating a 3D-model of each tumor half. The step size of the 3D motor was set to 63.5 µm. For each tumor half, the position of the two end points of the sample was manually recorded into the software (Vevo2100, VisualSonics).

3.4.4 Image analysis

Ultrasound images were analyzed using FIJI and MATLAB. An illustrated explanation of the image analysis process is included in Appendix B. First, all the images from one tumor half were treated as a stack of images in the z-direction. The entire stack of images was rotated so that the gel embedding around the tumor in the middle image of the stack became level. [1] Next, to make the task of individually analyzing each image in the image set manageable, every third image in the z-stack were kept and the rest discarded. This gave a z-resolution of 190 µm, which was considered acceptable for the purpose. The stack was then split into separate images and the rest of the image analysis was performed on each image separately.

The exposed surface of the tumor was marked by drawing a rectangle from the leftmost point where the tumor broke the gel surface, encompassing the entire exposed surface. The x-value of the leftmost point where the tumor broke the gel surface was noted. The image was then cropped to contain only the marked rectangle. Next, the image was thresholded according to the IsoData thresholding algorithm [50]. This rendered a binary image where all pixels defined as tumor were assigned the value 255, and all other pixels were assigned the value 0. The IsoData algorithm was chosen after careful consideration of several different algorithms applied to several images, as this was the algorithm that rendered the closest imitation of the original image of the tumor surface.

The text image resulting from the thresholding was analyzed: for each column, the number of pixels with a value of 0 entered before the first pixel with the value of 255 was counted. This number was then subtracted from the height of the image (height of the column) to give the height of the tumor surface above the cut surface in pixels. Counting from above was done in order to ensures that any pixels with value 0 inside the tumor did not cause it the tumor to be registered as lower than it was. The result of this analysis was a a vector of z-values, the height of the tumor surface above the gel surface, determined by the leftmost point where the tumor broke gel surface.

From each image, the vector of z-values was added to a matrix. According to the previously noted x-value of the point where the tumor broke the gel surface (i.e. the point where the vector should start), each vector was moved relative to the others by adding zeros before the first value. The final matrix with the vectors from all images was used to make topographic plots of the each tumor surface.

3.4.5 Construction of surface plots

Surface plots (SP) were created for each tumor half from the final matrix of z-value vectors for the US image analysis. In the SPs, different colors represented different height levels, which correlated with level of SS release. These levels were ranged from 0 to 4 according to height in pixels, as presented in Table 3.3.

[1] One tumor half, 8A, exhibited torsion, meaning that one part of the tumor was tilted differently than the rest. For this part of the tumor only, each image was rotated so that the gel appeared level. The additional rotation needed ranged from 3° to 9°.

Table 3.3: Levels of SS release found in SPs, in pixel height and height in µm

Level	SS release	pixels	µm
0	Zero	0	0
1	Low	1-9	1-277
2	Medium	10-19	278-555
3	High	20-29	556-833
4	Very high	>30	>834

3.4.6 Artifact removal

Artifacts such as noise, reverberations and ring down artifacts were present in regions of interest in a relatively large share of the images. Removal of artifacts was done for each image by changing the value of the pixels in question to 0, see Figure 3.5 for an illustration. Images with artifacts in the tumor surface that were impossible to remove without altering the image of the tumor, were discarded from analysis.

An overview of the image basis for this part of the project is given in Appendix D. For some of the tumor halves, the artifacts were of such an extent or character that all the images from the tumor half were discarded from quantitative analysis. However, for some of these tumors, a SP was constructed and used only for qualitative analysis.

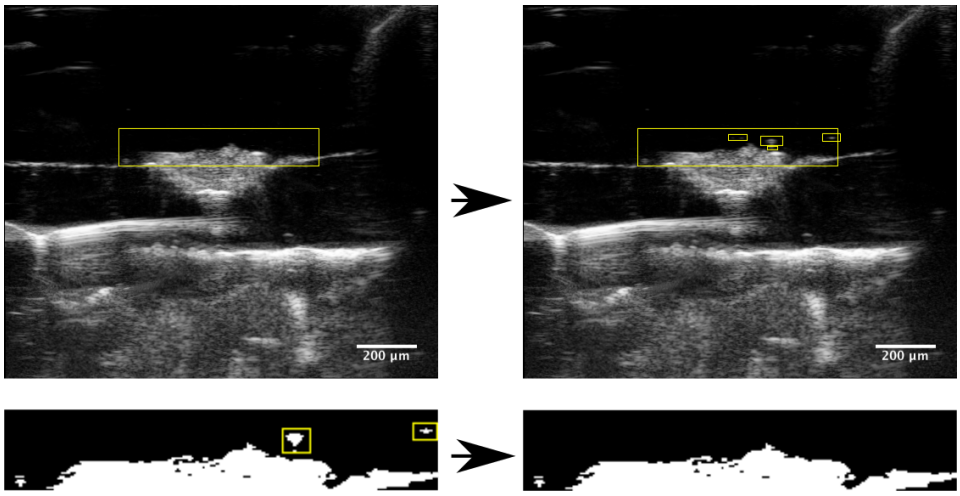

Figure 3.5: Illustration of artifact removal in image analysis of US images. A: Artifact removal before thresholding. Three artifacts are visible within the region of interest. B: Artifact removal after thresholding. Two artifacts are visible. The artifacts are manually removed by changing all pixel values to 0 in a small area including the artifact. Scale bars: 200 mm

3.4.7 Statistical analysis

Statistical data analysis was executed in Microsoft Excel. Data are presented as mean±SD. The data were assumed to apporximate a normal distribution. Heteroscedastic student t-tests were used to determine significance of the results. Correlation coefficient was determined with Pearson correlation tests, as a low number of outliers were present.

3.5 Effect of solid stress on nanoparticle delivery

3.5.1 Mounting of tumor sections

Tumor sections were kept frozen at $-80°$C before imaging. Application of mounting medium (VECTASHIELD) with DAPI fluorescent stain was applied upon thawing. The sections were then covered with a cover glass (VWR), which was sealed using nail polish. Subsequent imaging was performed immediately to avoid mobilization of NPs and/or dye in the mounting medium ["Nanoparticle microdistribution in tumor tissue: a characterization of a drug delivery system based on microbubble cavitation" by the author, 2017]. Imaging was performed in room temperature.

3.5.2 Tile scan imaging

Tile scans were obtained of the tumor section closest to the cut surface of the tumor half. This was done in order to provide a CLSM scan that would correlate closely with the SPs of SS measurements obtained from Section 3.4. In a few cases, the top tumor section was obstructed by the planar cut method, and the second or third highest was chosen. Appendix D provides an overview of which tumor section was used for the tile scan, along with the number of tiles for each section.

A CLSM Zeiss LSM800 was used to obtain tile scans of the tumor sections in this part of the project. The imaging settings used can be found in Table 3.4. A 20× objective with NA 0.5 was used with a magnification of 0.7. Images were obtained with a frame size of 1024×1024, with a scan speed of 485 487 pixels/s. Bidirectional scanning was applied and no averaging was used.

The tile scan was set up by tracing the outline of the tumor section in channel 1 (nuclei) and marking the peripheral points of the tumor. Furthermore, a focus surface was calculated by placing 9 focus points throughout the tumor section, thus obtaining a parabolic saddle focus surface. When finding the focus in these 9 points, both channel 1 (nuclei) and channel 2 (blood vessels) was taken into account, but not channel 3 (NPs).

Table 3.4: Imaging settings used for the tile scans obtained for tumor sections in the "Effect of solid stress on NP microdistribution" part of the project. Channel 1 imaged cell nuclei stained with DAPI, channel 2 imaged vascular endothelial cells stained with lectin-FITC and channel 3 imaged NPs stained with NR668. The pinhole size was chosen in order to obtain an optical section with thickness 6 µm.

Channel	1	2	3
Laser wavelength	405 nm	488 nm	561 nm
Laser intensity	1.8%	0.2%	2.5%
Detector range	400-520 nm	410-545 nm	553-627 nm
Detector gain	700V	600V	800V
Pinhole size	1.92 AU	1.67 AU	1.40 AU

3.5.3 Image analysis

Image analysis was performed in FIJI. An illustrated explanation of the image analysis process for this part of the project is found in Appendix C. To analyze the tile scans in this part of the project, they were aligned with the SP from the US images described in Section 3.4. This was done by rotating the surface plot to align with the directions of the tile scan, as explained in Figure 3.6. Both the SP and the tile scan was cropped to only contain the tumor. From the stack of US images, it was determined if the tumor extended beyond the SP, something which would be the case if the tumor had extensions beneath the gel surface. If this was the case, the extension was calculated from pixel size, and the tile scan was cropped to correspond with the right size of the SP. The SP was then scaled to the same size as the tile scan. This was done in order to be able to fit ROIs from the SP to the tile scan.

Using the "wand (tracing) tool" in FIJI, any region of the SP could easily be marked as an ROI, and placed on the tile scan. As explained in Section 3.4, every region on the SP represented a height range in µm by which the tumor surface rose over the cut surface after the planar cut method. By combining the ROIs in the tile scan and erasing everything outside the ROIs, an analysis could be performed for one specific level of SS (Table 3.3) at a time.

The subsequent analysis for each region of the tile scan was the same as the analysis described in Section 3.3.3 and illustrated in Appendix A, with the exception of which pixel threshold algorithms were used. For the tile scans, the "Moments" algorithm [51] was used in the blood vessel channel, and the "RenyiEntropy" algorithm [52] was used in the NP channel. The choice of these two algorithms was made after a systematic and careful consideration of several different algorithms for pixel thresholding.

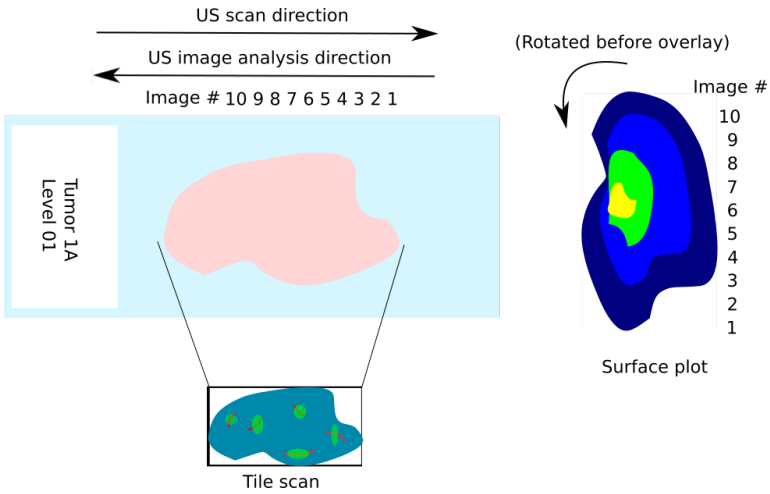

Figure 3.6: Illustration of the directionality of US imaging for creation of SPs and CLSM imaging of tile scans. The stack of US images was acquired from left to right. These images were analyzed in reversed order, and the SP was constructed from the bottom starting with the first image. This caused the SP to be rotated 90° to the right in relation to the tumor section. The tile scan was acquired with the same directions as the tumor section. Therefore, the SP was rotated 90° to the left to align it with the tile scan.

3.5.4 Artifact removal

The same method of artifact removal was used for the data from the tile scans as for the data in section 3.3.3.

3.5.5 Statistical analysis

NP density was measured in share of the pixels in the tile scan defined as NPs, divided by area fraction occupied in the SP, for each level. Data that corresponded with levels of SS that occupied less than 0.5 % of the area in the SP, were excluded from analysis of NP density, to avoid obscuring the data. Extravasation was measured as the fraction of the pixels defined as NPs found outside blood vessels in a level. ECM penetration was measured in average distance from a NP to the nearest blood vessel wall for a level.

Data analysis was executed in Microsoft Excel. Data are presented as mean±SD. The data were assumed to approximate a normal distribution. Heteroscedastic student t-tests were used to determine significance of the results. Correlation coefficients were determined with Spearman's rank correlation tests, as a relatively high number of outliers were present.

Chapter 4

Results

4.1 Summary of results from earlier studies

This section provides a summary of the results from the Specialization Project "Nanoparticle microdistribution in tumor tissue: a characterization of a drug delivery system based on microbubble cavitation", conducted by the author fall 2017. These results are derived from examinations of PC3 tumor tissue. The methods used to obtain these results are identical to those described in Section 3.3, and the results are directly comparable to the results presented in Section 4.2, in which OHS tumor tissue is examined.

The treated group showed a 97.8 %, significant (p=0.0005, t-test), increase in total NP accumulation, a 14.6 %, significant (p=0.033, t-test), increase in NP extravasation, and a 32.2 %, significant (p=0.0048,t-test), increase in NP penetration of the ECM compared to the control group. Illustrations of the results with details are given in Figures 4.1, 4.2 and 4.3.

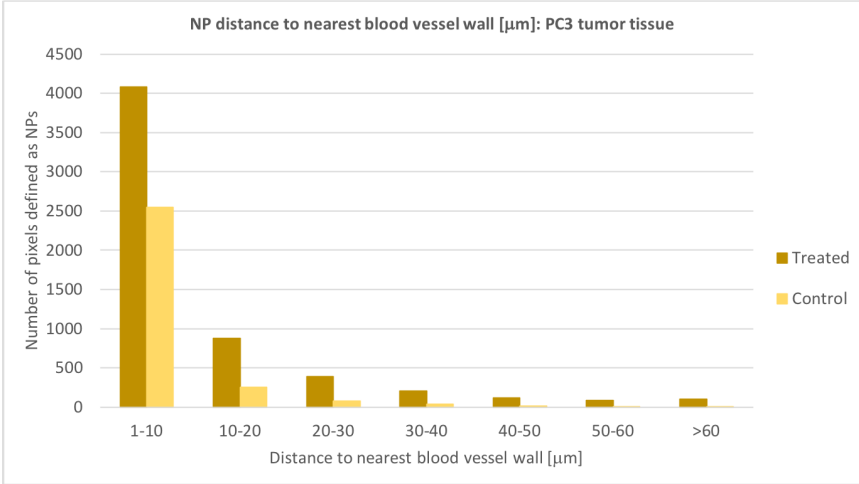

Figure 4.1: Histogram of nanoparticle distances to nearest blood vessel wall, in treated (brown) and control (yellow) samples of PC3 tumor tissue. The histogram has been normalized according to the number of images in each group (98 in control, 112 in treated). In the treated group, 2.3±2.8 % of pixels were defined as NPs, compared to 1.1±1.6 % in the control group. The distance average distance from NP to nearest blood vessel wall was 12.8±9.2 µm in the treated group and 9.7±6.6 µm in the control group. NPs with distance 0 (i.e. inside blood vessels) were not included when calculating ECM penetration.

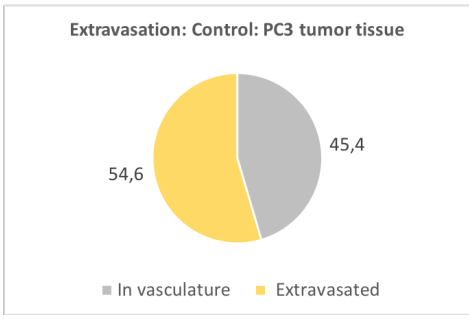

(a) Percentage of NPs inside (grey)/outside (yellow) blood vessel in the control group of PC3 tumor tissue. 54.626.0 % of the NPs were extravasated in this group.

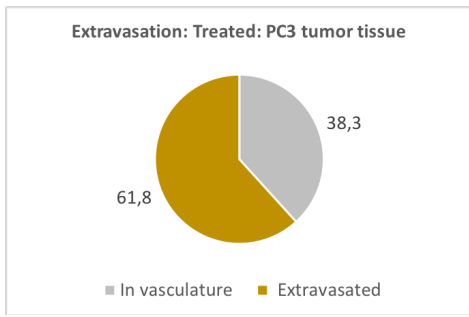

(b) Percentage of NPs inside (grey)/outside (brown) blood vessels in the treated group of PC3 tumor tissue. 61.825.0 % of the NPs were extravasated in this group

Figure 4.2

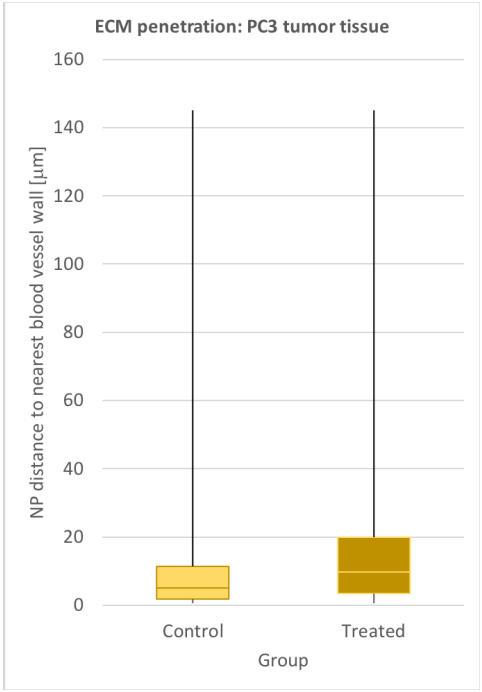

Figure 4.3: Box plot of distance from NP to nearest blood vessel wall in PC3 tumor tissue. Control (yellow): Median 5.12 µm, first quartile 1.71 µm, third quartile 11.37 µm, min distance 0.57 µm and max distance 145.03 µm. Treated (brown): Median 9.67 µm, first quartile 3.41 µm, third quartile 19.91 µm, min distance 0.57 µm and max distance 145.03 µm. NPs with a distance of 0 (i.e. inside blood vessels) were not included in this plot.

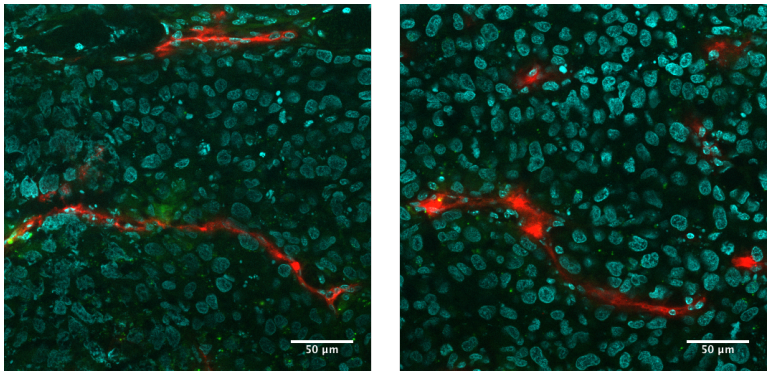

Figure 4.4: Representative HR CLSM images of the NP microdistribution in OHS tumor tissue. Left: Control group. Right: Treated group. Scale bars 50 µm.

4.2 Microdistribution of nanoparticles in OHS tumor tissue

In this section, results from the analysis of the microdistribution of NPs in OHS tumor tissue are presented. Typical examples of CLSM images of NP microdistribution from the control and treated groups of OHS tumor tissue are displayed in Figure 4.4.

4.2.1 Nanoparticle accumulation

A higher amount of pixels were defined as NPs in images from the treated samples compared to the samples from the control group, but the difference was not significant. In the treated group, an average of 2.2±2.3 % of each image was defined as NPs, while in the control group, this value was 1.9±2.8 %. Thus, the images from the treated group had an average NP content that was 18.0 % higher than the images from the control group. There was a large degree of inter-tumoral variation, as seen from Figure 4.5. The p-value was 0.3.

4.2.2 Nanoparticle extravasation

A significantly higher amount of the pixels defined as NPs were outside of blood vessel walls in the images from the control group, compared to images from the treated group, as illustrated in Figure 4.10. An average of 79.5±14.2 % of the pixels defined as NPs in images from the control group were outside blood vessel walls, compared to an average of 73.1±17.5 % of the pixels in images from the treated group. The treated group showed, in average, a 8.0 % decrease in extravasation. The p-value was 0.002.

An analysis of the NP extravasation in OHS tissue from lower resolution tile scans was performed to compliment the HR CLSM analysis. These results are presented in Appendix G.

4.2.3 Nanoparticle penetration of the extracellular matrix

The average distance from a pixel defined as a NP to the nearest blood vessel wall were similar for images from treated and control groups. The images in the treated group showed an average distance of 12.9±7.2 µm between NPs and blood vessel wall, and the images from the control group showed an average distance of 13.1±4.7 µm. This equated to a difference of 1.2 %. The p-value was 0.8, thus the difference was not significant. A box plot with median and quartile values for the ECM penetration in both groups is given in Figure 4.9.

The similarity in ECM penetration between groups was also present when counting only NPs with a distance of 40 µm or more from the nearest blood vessel. From this selection, the average distance between NP and the nearest blood vessel wall was 50.6±9.2 µm in the treated group and 49.6±6.3 µm in the control group. The p-value was 0.37, meaning the 2.0 % difference was not significant.

4.2.4 Correlation between extravasation and extracellular matrix penetration

Both groups showed a positive correlation between NP extravasation and penetration of the ECM. The treated group had a Spearman's rho value of 0.46 and the treated group had a Spearman's rho value of 0.56. The trend lines for the correlation were similar for the two groups, as shown in Figure 4.8.

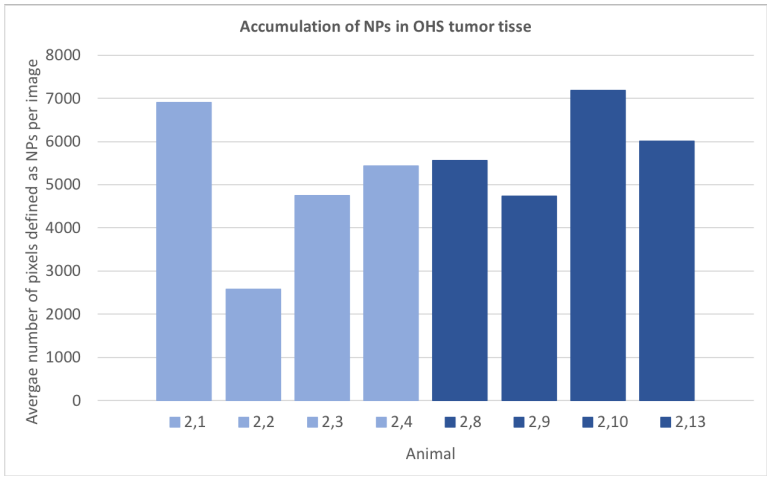

Figure 4.5: Bar plot of the NP accumulation in OHS tumor tissue for all 8 test animals. Control group in light blue, treated group in dark blue. NP accumulation was measured in average number of pixels defined as NPs in each image for each tumor. A large inter-tumoral heterogeneity was seen, especially in the control group.

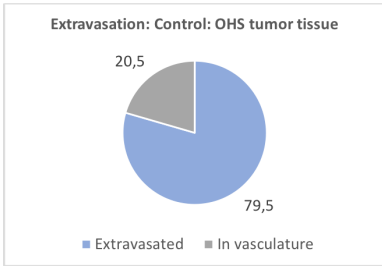

(a) Percentage of NPs inside (grey)/outside (light blue) blood vessel in the control group of OHS tumor tissue. 79.514.2 % of the NPs were extravasated in this group.

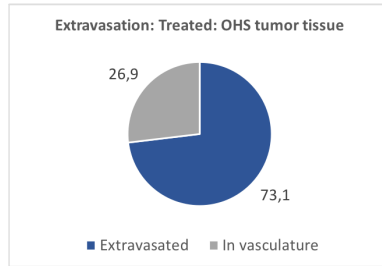

(b) Percentage of NPs inside (grey)/outside (dark blue) blood vessels in the treated group of OHS tumor tissue. 73.117.5 % of the NPs were extravasated in this group.

Figure 4.6

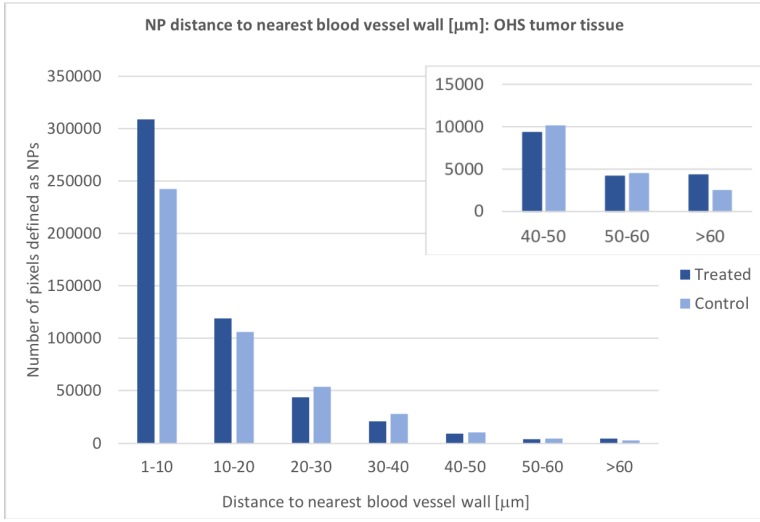

Figure 4.7: Histogram of NP distances to nearest blood vessel wall, in treated (dark blue) and control (light blue) samples of OHS tumor tissue. The histogram has been normalized according to the number of images in each group (117 in control, 119 in treated). NPs with distance 0 (i.e. inside blood vessels) were not included in this histogram.

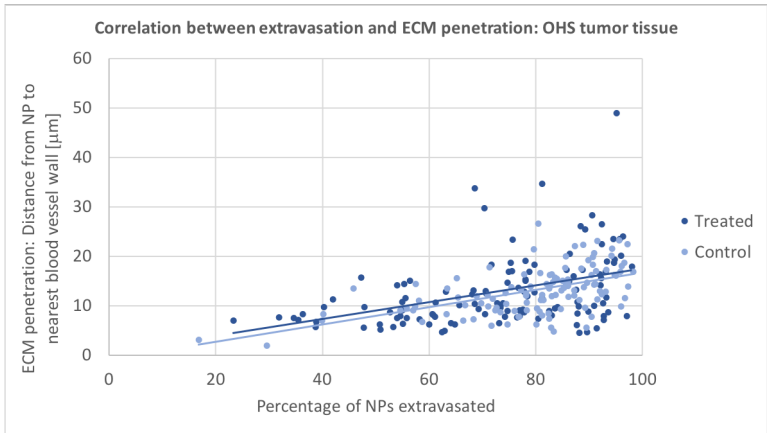

Figure 4.8: Correlation between extravasation of NPs and mean distance from NP to nearest blood vessel wall in OHS tumor tissue. Trend lines for each group are displayed. Treated samples are shown in dark blue, and control samples in light blue. Spearman's ρ treated group: 0.46 and control group: 0.56. Trend line formula treated group: $y = 0.17x + 0.55$ and control group: $y = 0.18x - 0.084$.. NPs with a distance of 0 (i.e. inside blood vessels) were not included in this plot.

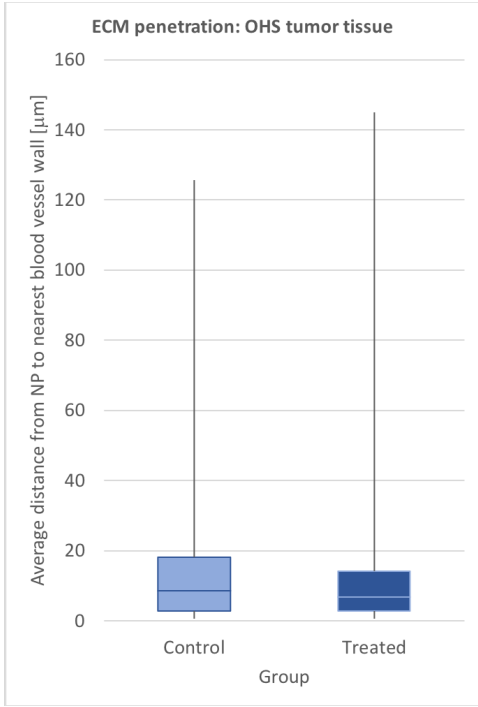

Figure 4.9: Box plot of distance from NP to nearest blood vessel wall in OHS tumor tissue. Control (light blue): Median 8.53 µm, first quartile 2.84 µm, third quartile 18.20 µm, min distance 0.57 µm and max distance 125.69 µm. Treated (dark blue): Median 6.82 µm, first quartile 2.84 µm, third quartile 14.22 µm, min distance 0.57 µm and max distance 145.03 µm. NPs with a distance of 0 (i.e. inside blood vessels) were not counted in this plot.

4.3 Comparison of nanoparticle microdistribution in OHS and PC3 tumor tissue

Based on the results from the Specialization Project presented in Section 4.1 and the data presented in Section 4.2 a comparison of the NP microdistribution in OHS and PC3 tumor tissue was performed. In addition, data from the tile scans (Section 4.4.3) of both tissue types were used to complement the comparison. To establish the difference in baseline NP microdistribution and EPR effect in these two tissues, only samples from the respective control groups were included in this analysis.

The NP accumulation was significantly higher in OHS tissue than in PC3 tissue. In high-resolution CLSM images, 1.9±2.8 % of the pixels were defined as NPs in OHS tissue, compared to 1.1±1.6 % in PC3 tissue. The difference of 64.9 % had a p-value of 0.01. When analyzing tiles cans, the NP accumulation was highly heterogeneous. Even though PC3 tumors showed a NP accumulation which was 322.9 % higher than that of OHS tumors, the difference was not significant (p=0.10,

t-test). In OHS tumors, 0.2±0.4 % of the total tile scan pixels were defined as NP, compared to 0.8±0.8 % in PC3 tumors.

NP extravasation was significantly higher in OHS tissue than in PC3 tissue, when analyzing high-resolution CLSM images. OHS tumors showed an average extravasation of 79.5±14.2 %, while the average extravasation in PC3 tumors was calculated to 52.9±25.3 %. The 50.3 % higher extravasation in OHS tissue had a p-value<0.0001. The same difference in NP extravasation could not be found from tile scan data, which showed only a 10.9 % increase in extravasation from PC3 (58.7±22.8 %) to OHS tissue (65.0±11.5 %). This difference was not significant with a p-value of 0.22.

NP penetration of the ECM was found to be significantly higher in OHS tissue than in PC3 tissue. In HR CLSM images of OHS tissue, NPs were found an average of 13.1±4.7 µm from the nearest blood vessel wall, compared to an average of 9.7±6.6 µm in PC3 tissue. This difference of 35.2 % had a p-value<0.0001. In tile scans, a smaller difference found of 12.5 %, with an average distance of 2.8±2.5 µm for OHS tissue, and 2.5±1.6 µm for PC3 tissue. However, this difference was not significant with a p-value of 0.57.

4.4 Release of solid stress

4.4.1 Surface plots from the planar cut method

SPs were generated from US images for 30 tumor halves: 15 from OHS tissue, and 15 from PC3 tissue. An array of 28 SPs is included in Appendix E; two SP lacked large parts of the surface due to image artifacts and were not included.

For tumor halves from OHS tissue, 14 out of 15 tumor halves (93 %) included at least one area of a high or very high level of SS release. In 4 of the tumor halves (25 %), there was one single area with a high or very high level of SS release approximately centered in the tumor. 7 out of 15 of the tumor halves (47 %) differed significantly from a typical perception of a tumor with one centered area with a high level of SS. 7 tumor halves (47 %) included moderately large areas with no release of SS. In Figure 4.10a, a typical SP of an OHS tumor half is shown.

For tumor halves from PC3 tumor tissue, 14 out of 26 (54 %) of the tumor halves did not include an area where the SS release was high or very high. 7 of the tumor halves (27 %) fitted with the perception of a tumor with one centered area with a high level of SS. The rest either lacked such an area, or it was located somewhere in the tumor periphery. 16 tumor halves (62 %) included large areas with no release of SS. Figure 4.10b, a typical SP of a PC3 tumor half is shown.

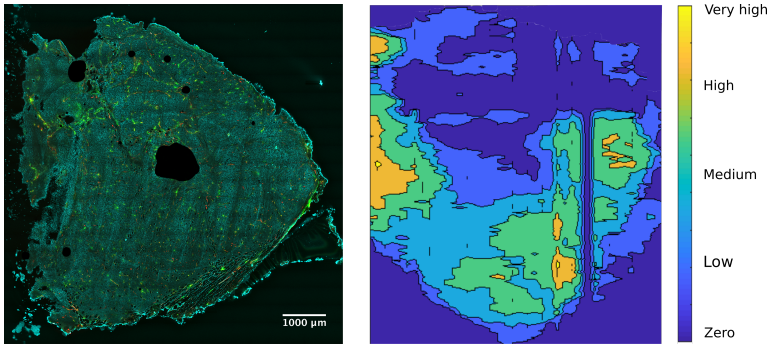

(a) The OHS tumor section is well-perfused by blood vessels. NPs are mostly distributed around blood vessels. The tumor half shows several areas with a high level of SS release. These areas are not necessarily centered in the tumor.

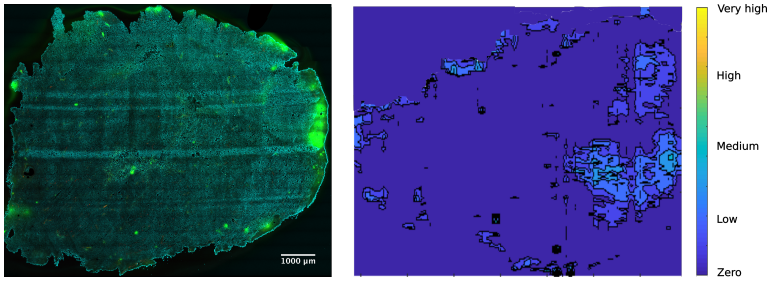

(b) The PC3 tumor section contains few visible blood vessels. NPs are mostly distributed around blood vessels, but several large "clouds" of NPs are visible in the tumor, mainly in the periphery. The tumor half consists mostly of areas with no SS release, with a few areas with a low level of SS release.

Figure 4.10: Left: Tile scans of typical OHS (a) and PC3 (b) tumor sections. NPs in green, blood vessels in red and cell nuclei in cyan. Note that the tile scans have been scaled to a lower resolution than the one used for analysis, and details will have been lost. Right: SPs of the distribution of SS in the tumor halves which the tumor sections originated from (OHS: 3A, PC3: 21B). Scale bars 1000 µm

4.4.2 Statistical analysis of the release of solid stress

OHS tumors showed a significantly higher release of SS than PC3 tumors. The surface of OHS tumors was measured to an average of 366.0±266.5 µm above the cut surface in the direction perpendicular to the cut, while the same value for PC3 tumors was 183.5±146.8 µm. The average release of SS was therefore 99.5 % higher in OHS tumors than in PC3 tumors. The p-value was <0.0001. Figure 4.11 shows the average increase in SS with standard deviation for the OHS and PC3 tumors, treated and control groups.

In OHS tumors, the control group showed a significantly higher release of SS than the treated group. The average expansion of the cut surface in the di-

rection perpendicular to the cut was 338.5±173.2 µm in the treated group, and 380.8±314.8 µm in the control group. Thus, the treated group showed a decrease in SS release of 11.1 % compared to the treated group. The p-value was 0.029. See Figure 4.11 for a visual representation of the SS release in OHS tumor halves. In Appendix F.1, data per animal are given for release of SS in OHS tumor halves.

In PC3 tumors, there was a significantly higher release of SS in the control group compared to the treated group. The control group showed an average height increase of 176.3±150.0 µm above the cut surface, while the control group showed an average height increase of 193.3±140.0 µm. The treated group showed an average release of SS that was 8.8 % lower than the treated group. The p-value was 0.030. See Figure 4.11 for a visual representation of the SS release in PC3 tumor halves. In Appendix F.2, data per animal are given for release of SS in PC3 tumor halves.

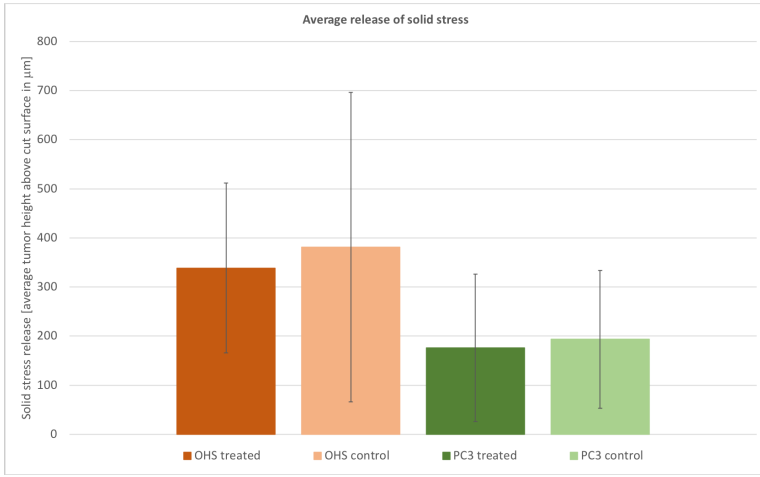

Figure 4.11: Average release of SS in OHS and PC3 tumor tissues, treated and control groups. Release of SS was measured according to the planar cut method, in tumor height above cut surface, in µm. Error bars equals SD for each group.

4.4.3 Correlation between tumor size and solid stress release

Correlation between tumor size approximated as mm in z-direction ×mm in x-direction and release of SS was measured, see Figure 4.12. For OHS tissue, the treated group showed a strong positive correlation with a Pearson's correlation coefficient (PCC) of 0.63, and the control group showed a positive correlation of 0.39. For PC3 tissue, both treated and control groups showed a positive correlation with a PCC of 0.37. The correlation was similar for both tumor types.

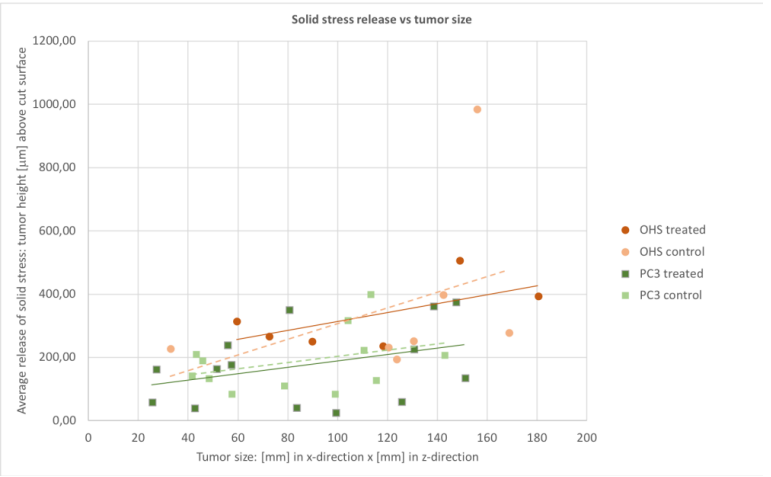

Figure 4.12: Average release of SS in correlation to tumor size, for OHS and PC3 tumor tissue, treated and control groups. Release of SS was measured according to the planar cut method, in tumor surface height above cut surface, in µm. Tumor size was approximated as mm in z-direction × mm in x-direction of the tumor. Dots represent OHS tumors and squares represent PC3 tumors. Treated groups in dark colors, control group in lights colors. Regression lines are solid for treated groups and dashed for control groups. Regression line formulas: OHS treated: $y = 1.4x + 172.5$, OHS control: $y = 2.5x + 59.9$, PC3 treated: $y = 1.0x + 88.3$ and PC3 control: $1.0x + 105.1$

4.5 Effect of solid stress on nanoparticle delivery

The data for this analysis were obtained from 28 tumor halves, 15 from OHS tumor tissue (7 treated, 8 control) and 13 from PC3 tumor tissue (7 treated, 6 control). An overview of the correlation between level of SS release and NP accumulation, extravasation and ECM penetration is given in Table 4.1.

Table 4.1: Spearman's ρ values for the correlation between level of SS release and NP accumulation, extravasation and ECM penetration, for OHS and PC3 tumor tissue, treated and control groups.

	OHS treated	OHS control	PC3 treated	PC3 control
Accumulation	-0.22	0.18	-0.14	-0.21
Extravasation	0.21	0.01	-0.37	-0.35
ECM penetration	-0.32	-0.32	-0.53	-0.52

4.5.1 Nanoparticle accumulation

The NP content in tumor tissue was examined in relation to the level of SS release in the same tissue sample. NP content was measured as (# of NPs in SS level/total # of NPs in tumor section) divided by (area of SS level/area of tumor section). In other words, a NP content of 1.00 would indicate that the specific level of SS release had a NP content expected by it's extension in the SP, if all NPs were evenly distributed across all levels. A NP content above 1.00 would indicate a higher accumulation of NPs, and a content below 1.00 would indicate a depletion of NPs, in the area corresponding to that level of SS release. Levels with area fractions below 0.5 % of the SP were excluded from this part of the analysis. The level of SS release was measured in tumor surface height in µm above the cut surface.

Figure 4.13 presents the correlation between average NP content and level of SS release in OHS and PC3 tumor tissue for all levels of SS release, for treated and control groups.

The accumulation of NPs showed a weakly negative correlation to the level of SS release for the OHS treated, PC3 treated and PC3 control groups, with Spearman's rho's of -0.22, -0.14 and -0.21, respectively. The control group of OHS tissue showed a weakly positive correlation between NP accumulation and SS release, with Spearman's rho of 0.18.

4.5.2 NP extravasation

Extravasation of NPs from the vasculature of OHS and PC3 tumor tissue was characterized and related to the level of SS release in the same tissue sample. The average NP extravasation related to level of SS release is presented in Figure 4.14. Extravasation was measured in the share of pixels defined as NPs found outside the blood vessels in tile scans.

The correlation between NP extravasation and level of SS release in OHS tissue was found to be weakly positive with a Spearman's rho value of 0.21 for tissue in the treated group. No correlation was found in the control group, which had a Spearman's rho value of 0.01.

In the OHS treated group, the areas with a medium level of SS release (level 2) had a significantly lower NP extravasation than the areas with the highest (level 4) and the lowest (level 0) level of SS release. In areas with level 2 SS release, the average NP extravasation was 65.9±0.1 %. This was 9.4 % lower than the extravasation in level 0 areas (72.7±0.05 %), and 11.9 % lower than the extravasation in level 4 areas (74.8±0.06 %). The p-value for the two differences were 0.026 and 0.0062, respectively.

For PC3 tumor tissue, a negative correlation was found between NP extravasation and level of SS release in both treated and control groups, with Spearman's rho values of -0.37 and -0.35, respectively.

In the PC3 treated group, the extravasation in areas with no release of SS was 30.4 % higher than the extravasation in areas with a very high release of SS, with 76.3±0.1 % of the NPs extravasated compared to 58.5±0.3 %. However, the

difference was not significant, with a p-value of 0.51.

Stronger result were seen in the PC3 control group: extravasation in areas with no release of SS were 69.0 % higher than that in areas with a very high release of SS, with 68.4±0.09 % compared to 40.4±0.2 % extravasation. Here, the p-value was 0.08, thus the difference was not significant.

4.5.3 Nanoparticle penetration of the extracellular matrix

The average ECM penetration of NPs related to level of SS release is presented in Figure 4.15.

In OHS tissue, the correlation between ECM penetration and level of SS release was negative for both treated and control groups, with a Spearman's rho value of -0.32 for both.

In the OHS treated group, the NP penetration of the ECM was 65.4 % higher in areas with no SS release, than in the areas with the highest level of SS release. While areas with level 0 SS release showed an average ECM penetration of 13.1±5.7 µm, level 4 areas showed an average penetration of 8.0±4.1 µm. The p-value was 0.20, thus the difference was not significant.

In the OHS control group, the NP penetration of the ECM was 43.3 % higher in the areas with the highest release of SS, compared to the areas of no SS release. Level 0 areas showed an average ECM penetration of 5.04±1.0 µm, and level 4 areas an average of 7.2±6.8 µm. The p-value was 0.63, thus the difference was not significant.

A negative correlation between level of SS release and NP penetration of the ECM was found in PC3 tumor tissue for both the treated and control groups, with Spearman's rho values of of -0.53 and -0.52, respectively.

In PC3 treated tissue, NPs in areas with no SS release, penetrated the ECM in average 275.2 % longer than NPs in areas with a very high level of SS release. The average ECM penetration in level 0 areas was 10.4±7.0 µm, while in level 4 areas the average was 2.8±0.2 µm. The difference was not significant, with a p-value of 0.10.

In PC3 control tissue, NPs in areas with no SS release showed an average ECM penetration of 7.1±2.1 µm, compared to 3.1±0.2 µm for NPs in areas with a very high level of SS release. This difference of 133.4 % was significant with a p-value of 0.049.

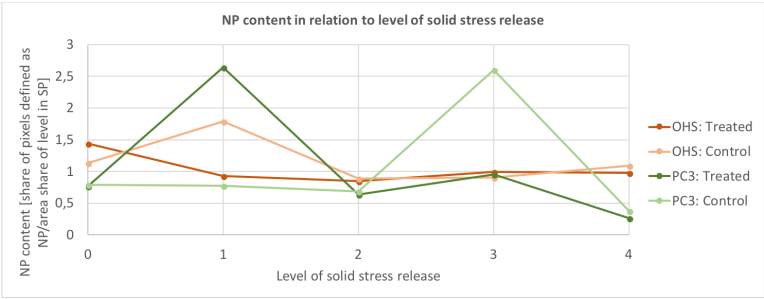

Figure 4.13: Average NP content relation to level of SS release in OHS and PC3 tumor tissue, treated and control. NP content was measured in share of pixels defined as NPs divided by share of SP occupied by level of SP release. OHS: Treated group in dark orange, control group in light orange. PC3: Treated group in dark green, control group in light green.

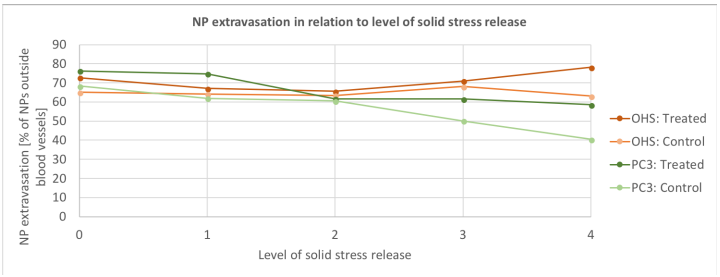

Figure 4.14: Average extravasation of NPs versus level of SS release in OHS and PC3 tumor tissue, treated and control groups. OHS: Treated group in dark orange, control group in light orange. PC3: Treated group in dark green, control group in light green.

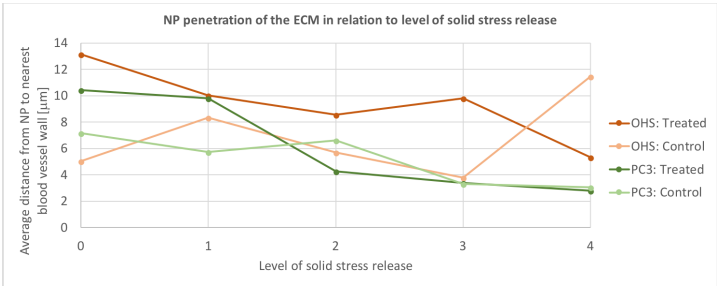

Figure 4.15: ECM penetration by NPs versus level of SS release in OHS and PC3 tumor tissue, treated and control. OHS: Treated group in dark orange, control group in light orange. PC3: Treated group in dark green, control group in light green.

Chapter 5

Discussion

This project was conducted at the department of physics at NTNU, division of biophysics and medical technology, as a part of a larger project revolving around the DDS in question. Several studies partly overlapping with some of the subjects investigated in this project have been published by this group [11, 12, 29]. Naturally, these publications have been important in the work involved this project. In addition, a Specialization Project conducted by the author presented results which are closely related to the work done in this project, namely the microdistribution of NPs in PC3 tumor tissue, in terms of accumulation, extravasation and ECM penetration. These results are summarized in Section 4.1.

5.1 Microdistribution of nanoparticles in tumor tissue

5.1.1 Comparison of nanoparticle microdistribution in OHS and PC3 tumor tissue

Using data from the image analysis of HR CLSM images of a random selection of blood vessels in both OHS and PC3 tissue, supplemented with data from the image analysis of slightly lower resolution CLSM tile scans of OHS and PC3 tissue, a comparison between the microdistribution of NPs in the two tissue types was done. The comparison was conducted on the control groups of both tissue types, to establish a understanding of the baseline microdistribution of NPs and EPR effect in the two tissues.

When analyzing HR CLSM images, the NP accumulation in OHS tissue was significantly higher than that of PC3 tissue. No significant difference was found from tile scans. OHS tumor tissue showed a significantly higher extravasation than PC3 tissue based on the HR CLSM images. The tile scans also showed a difference in extravasation between the two, but this was not significant. OHS tissue exhibited a higher ECM penetration based on both HR CLSM images and tile scans, a finding which was significant in the HR CLSM images.

Together, these comparisons prove that OHS tumor tissue has a larger baseline EPR effect than PC3 tissue, with a higher accumulation, extravasation and ECM penetration of NPs.

Considering that OHS tissue is better perfused with a higher density of blood vessels than PC3 tissue [53], a higher accumulation of NP here was expected. This simply follows from the fact that more blood vessels have the capacity to carry a higher amount of NPs. The method of analyzing NP accumulation in a selection of HR CLSM images, all including blood vessels, should not be considered a suitable method for analyzing NP content in different tissue types. This follows from the obviously biased selection of images, as tumor areas with no blood vessels would show less NP accumulation if they were imaged. Here, the tile scans did not contain data which was able to elaborate the understanding of NP accumulation, because of a large degree of inter-tumoral heterogeneity. Even so, the higher vascular density in OHS tumor tissue could be argued to be an individual marker for higher NP accumulation, until this issue is further investigated.

The higher grade of NP extravasation in OHS tissue can also be explained by the differences in vasculature between the two tissues. Sulheim et al. [53] found that the MB inflow time was much higher in OHS than in PC3 tumor tissue. They reasoned that because of the relatively large size of MBs, a long inflow time was caused by MB retention in the vasculature, which would be caused by chaotic microvasculature with twists and dead ends. Assuming that this was indeed the case for the vasculature in OHS tissue, it would be reasonable to assume that the chaotic nature of the vasculature also encompassed a higher degree of leakiness in the vascular walls, which would enable easier NP extravasation.

Finally, the increased ECM penetration in OHS tumor tissue can not be explained by the tumor microenvironment. On the contrary, the microenvironment in OHS tumors include a higher cell density [53] and a higher level of SS, and therefore a higher amount of ECM components, than PC3 tissue. These factors would intuitively lower the ability of NPs to penetrate the ECM. However, ECM penetration was found to correlate positively for both OHS and PC3 tissue (data not shown). Therefore, it may seem like the most significant barrier for NPs is that of the vascular walls, and the higher ECM penetration in OHS tissue might simply have followed from the higher degree of extravasation. This claim is supported by the fact that the difference in extravasation between the two tissues was larger than the difference in ECM penetration.

5.1.2 Effect of ultrasound on nanoparticle microdistribution in OHS tumor tissue

The total accumulation of NPs was higher in the treated group of OHS tissue compared to the control group, but the difference was not significant. This could be an indication that the US treatment had a positive effect on NP accumulation in the tissue and blood vessels.

Increased NP accumulation in tumor tissue after treatment with MB cavitation has been reported previously by our group [11, 12] and others [54, 55, 56, 57].

Therefore, this result is in agreement with previous results on this point.

It has been documented that the systems with high intensity US [54], or a higher MI [11, 12] have been the most successful in increasing NP accumulation in tumor tissue, compared to systems using lower intensity or lower MI US. This is a strong indication that MB destruction is beneficial for accumulation compared to stable cavitation. During inertial cavitation, effects like microjets and shock waves arise, in addition to ARF, microstreaming and MB expansion pushing on vessel walls, which are also present during stable cavitation. During the treatment used here, MB cavitation was not monitored to ensure inertial cavitation, but total MB destruction was expected from the treatment [11].

Higher NP accumulation has been shown for complexes where the NPs are conjugated to the MBs, like in the DDS described here, than for NPs co injected with MBs [54, 57], where these two groups have been compared. Seen in connection with the positive effect of inertial cavitation, it is natural to conclude that the increased effect of directly associating the NP to the MBs is a result of NPs being affected by the forces involved in inertial cavitation.

The circulation half-time of the NPs used in this project was previously characterized by our group to 136 min [11]. The animals used for the characterization of microdistribution of NP in OHS tumor tissue were sacrificed after 6 h, ensuring that NPs would be cleared from circulation. This leads to the assumption that the NP accumulation seen here consists of NP either in the ECM, deposited along the vascular walls or taken up by vascular endothelial cells. To separate the former from the two latter, the extravasation of NPs was quantified by analyzing the share of NP fluorescence overlapping with blood vessels in CLSM images.

The treated group showed a significant decrease in extravasation of NPs compared to the control group. This indicates that for OHS tumor tissue, the US treatment caused fewer NPs to extravasate. This was an unexpected result, and the opposite effect of what was seen for PC3 tissue (Section 4.1), and what has been reported by others [11, 12, 57] (MDA-MB-231, PC3 and Rat C6 Glioma tumor tissue, respectively) using a similar or identical DDS.

The reason behind this unexpected result is probably to be found in the vascular properties of OHS tumor tissue, combined with the relatively long time period before euthanization of the animals (6 h).

First, unlike PC3 tissue, OHS tissue is well perfused, with a high volume of functioning blood vessels and no large necrotic areas[53]. This is true throughout the tumor, whereas in PC3 tissue, blood vessel concentration is much higher in the periphery [53]. Along with the results already presented here, this is a strong indication that the EPR effect in OHS tissue is stronger than in PC3 tissue. Keeping in mind the tendency towards increased accumulation of NPs in the treated tissue, an explanation to the decreased extravasation upon US treatment could be a high degree of NP uptake in blood vessel endothelial cells after sonication. The treatment used here has indeed been shown to increase cellular uptake of the NPs [58]. This effect would be enhanced by NPMBs being pushed against the capillary walls by ARF, as theorized by others [11, 12, 23]. NPs that were endocytosed by endothelial cells would probably be impaired from further extravasation, explaining

why this parameter was decreased upon treatment.

Others [11] have pointed to increased endothelial cell endocytosis of NPs as a contributing reason behind *increased* extravasation, but with the quantification method used here, these NPs would register as non-extravasated. Burke et al. [57] also reported increased colocalization between NPs and BS-1 lectin upon sonication, indicating endothelial endocytosis of the particles. In tissue types with a lower baseline EPR effect, the increase in accumulation might be larger and more significant upon treatment (as seen in PC3 tissue), and the effect of endothelial endocytosis of the NPs would probably be counteracted by increased permeability of the blood vessels as a result of jet streams from MB collapse, and therefore not visible in the results.

The relatively long time period between injection of NPs and euthanization of the animals, 6 h, compared to the circulation half life of the particles, 136 min, should be considered a flaw in the experiment set up for characterizing the degree of NP extravasation. As mentioned above, NPs would have been cleared from circulation at the time of euthanization, which means that the NPs registered in the images were either deposited along vascular walls, taken up by vascular endothelial cells, or extravasated, while no NPs would have been present in the blood.

To partially amend the experimental flaw explained above, tile scans of OHS tumors from animal Trial 2 and 3 where the time between injection and euthanization was 30 min, were analyzed, see Appendix G. In these tumor sections, NPs would be present in the blood. Here, the treated group showed a significant increase in NP extravasation compared to the control group. This indicates that the US treatment did in fact have a positive effect on the extravasation, as expected and previously reported. This positive effect was likely caused by MB collapse inducing microjets and shock waves able to generate pores in the vascular walls and increase the permeability of these [8, 9, 10]. However, the tile scans had a lower resolution than the HR CLSM images originally analyzed, and a lower grade of NP extravasation was found for both treated and control groups from analysis of the tile scans compared to the HR CLSM images. In conclusion, the parameter of NP extravasation should be further analyzed with HR CLSM images of tumors with a shorter time period from NP injection to euthanization.

The average distance from an extravasated NP to the nearest blood vessel wall was similar between treated and control groups: the treated group showed a non-significant decrease of 1.2 % in ECM penetration. When only analyzing the NPs with an ECM penetration of 40 µm or more, the groups were also similar. This indicates that for OHS tumor tissue, US treatment has little or no effect on the ECM penetration of NPs. Again, this result is not consistent of what is found for PC3 tissue by the author (Section 4.1), and for PC3, A431 and BX-PC3 by others [12, 56].

Sulheim et al.[53] reported significant differences between OHS tissue and several types of carcinomas including PC3 which can explain why MB cavitation gave increased ECM penetration by NPs in the latter, but not in the former. First, the OHS tissue was reported to be well perfused throughout the tumor and without large necrotic areas. A large number of functioning blood vessels would lead to a

greater blood flow trough the tumor, facilitating the leakage of fluid into the tumor interstitium and elevating the IFP, thus preventing efficient interstitial transport of NPs. US treatment would probably not alter this feature of OHS tumor. Second, they reported a high cell density in OHS tumors compared to a low cell density in PC3 tumors, a parameter which correlated with diffusivity and would naturally obstruct ECM penetration. Again, US treatment would probably not affect the cell density to a significant degree. Considering that significant hindrances to ECM penetration are inherent of OHS tissue, and that these hindrances were probably not alleviated by US treatment or MB cavitation, this could explain why the treatment did not prove effective for this specific parameter.

Eggen et al. [12] reported a significant reduction in ECM penetration by NP in the central parts of the tumor after high MI sonication, using PC3 tumor tissue. They explained this by the high IFP present in central parts of tumors, an explanation which is consistent with the explanation above.

A positive correlation was found between NP extravasation and ECM penetration in both groups of OHS tumor tissue. The correlation was similar for both groups, a finding which is in accordance with the hypothesis that the US treatment had little to no effect on the ability of NPs to penetrate the ECM.

Interestingly, Theek et al. [56], concluded that their DDS with US appeared to be independent of tumor model. This conclusion was based on the fact that they saw increased accumulation and improved microdistribution for two tumor models with different properties: A431 with a blood volume of 1.8 % and Bx-PC3 with a blood volume of 2.7 %. Sulheim et al. [53] reported a blood volume of 0.25 % in PC3 tumors and 1.6 % in OHS tumors. Note that methods of blood volume quantification were not the same between the two papers and are not directly comparable. Nonetheless, the difference between the blood volume of the two tumors described in this thesis is larger than the one described by Theek et al. Our results therefore prove that a DDS based on inertial cavitation of MBs associated to NPs is, in fact, not independent of tumor model. While the DDS with US provided significantly increased accumulation and improved microdistribution in PC3 tissue, the same effect was not seen for OHS tissue.

5.2 Release of solid stress

The "Planar cut method" for releasing and measuring SS was first described by Nia et al. in 2016 [13]. Previous to this, SS was considered challenging to measure, and mathematical models were relied upon in place of experimental methods. Thus, the planar cut method provides a simple and reliable method of releasing and measuring SS that can compliment and elaborate on mathematical models.

Nia et al. [13] reported no deformation following the planar cut method for tissues which were expected to hold an insignificant level of SS, i.e. healthy kidney and liver tissue. This was considered sufficient proof that the method did indeed measure SS, and we did not consider it necessary to repeat these control experiments for healthy tissue.

SS consists of two components: external SS arising from the tumor boundary

regions pushing against in confinements (i.e. healthy tissue) and residual SS, arising from tumor growth. When harvesting the tumor and thus removing it from its confining tissue, the external SS is eliminated. This fact was confirmed by Nia et al. when comparing the *ex vivo* planar cut method to the *in vivo* "Needle Biopsy method" and finding a smaller deformation from the planar cut method [13]. Therefore, it is only the residual SS which is characterized by the project described in this thesis.

When characterizing the spatial distribution of SS in tumors, it has been the standard to assume a distribution with a relatively high compressive SS in the tumor centre, and lower, or even tensile SS in the tumor periphery [13, 59]. This assumption has prepared the ground for an understanding of DDSs where it has been natural to differ between the microdistribution in the tumor centre and periphery [12]. Although several other important characteristics of tumor centre vs. periphery are valid, like IFP, necrosis, and perfusion, this project aimed to illuminate whether SS typically is, in fact distributed in accordance with this assumption.

Through a qualitative assessment of 41 SPs from tumor halves from PC3 and OHS tissue, it can be concluded that SS does not, in fact, show the typically assumed distribution for all tumor types. 73 % and 53 % of the tumor halves of PC3 and OHS tissue, respectively, did not fit the proposed distribution. This result is in compliance with the SS profiling of U87 tumors performed by Nia et al., but not with that of MM3V-MTC and AK4.4 tumors [13]. In conclusion, tumor heterogeneity is present to a high degree for the parameter of SS like for many others, and there is reason to believe that it would be beneficial to characterize the SS profile of a specific tumor type, or even for each tumor like in this thesis, when working with a DDS.

Based on image analysis of US images of 39 tumor halves exposed to the planar cut method, a quantitative analysis of the solid stress release in PC3 and OHS tumors was performed. OHS tumor tissue showed a significantly higher level of SS release than PC3 tumors. This is in accordance with the fact that OHS tissue has a higher density of cells [53], and therefore also a higher content of ECM components produced by cells than PC3 tissue, both causing increased levels of SS [59].

The statistical analysis of US images also revealed that US treatment combined with NPMBs significantly lowered the release of SS in these tumors. This proves that our DDS in combination with US has the potential to reduce the residual SS level in tumors. It has been shown that a high level of SS can impair drug delivery by i.e. compression of blood and lymphatic vessels and thereby preventing accessibility to the entire tumor [59]. A high level of SS has also been shown to enhance tumor progression [13] and even induce malignant behaviour in healthy cells in the tumor proximity [60].

To the best of the author's knowledge, it has never before been suggested that US treatment alone or combined with cavitation of MBs has the potential to decrease the level of SS in tumors, and it is therefore not possible to find support in the literature as to the reasons behind this effect. Previous descriptions of SS reduction involve depletion of cancer cells, fibroblasts, collagen or HA, or a combination of these [59].

US alone [61] or in combination with MBs [62, 63] has been shown to induce apoptosis in cells. This could possibly be the reason behind the lower SS levels in the treated group. However, apoptosis induction has, to the best of the author's knowledge, not been shown for an US treatment of only 2 min, as the one used here. To determine if this was the reason behind lowered SS levels, this specific treatment would need to be characterized in terms of cell viability.

Previous evidence from our group suggest that the collagen amount of tumors is not affected by the treatment [12], although this is inconclusive and does not take collagen structure into account, and should therefore be investigated further. Pirentis et al. [20] point to the fact that collagen contributes to the generation of SS only in the periphery, whereas in the tumor centre, the fibers are slackened due to compressive stress. Therefore, the altering of collagen is probably not the reason behind lowered SS in the treated group.

The depletion or collapse of HA networks is left as the perhaps most plausible explanation to the decrease in SS stress upon treatment. This is a feature which could be investigated relatively easily in future experiments, by for example immunostaining of the tissue.

In addition to causes involving apoptosis or HA networks, a possible explanation for the decrease in SS involves the already well documented effect that inertial MB cavitation have on blood vessels and vascular endothelial cells [11, 55, 56, 57, 58]. It is possible that the creation of pores either in the membranes of endothelial cells, or the basement membrane of the vascular network, caused a collapse of one or both of these structures, which was able to free up space in the tumor and thereby release SS. A collapse of blood vessels due to perforation of the basement membrane would not be visible by the methods used here, as vessels were labeled with lectin after the US treatment was terminated. Labelling blood vessels with immunostaining in addition to lectin and analyzing the difference between groups would illuminate this possibility. A possible collapse in endothelial cell membranes would need to be investigated further in CLSM images with higher resolution than the ones analyzed here.

Quantitative analysis revealed that for PC3 and OHS tumors, treated and control groups, the level of SS release increased with tumor size. This is in consistence with previous results [13, 59] and indicates that the residual component of SS in tumors is growth induced and accumulates with size.

5.3 Effect of solid stress on nanoparticle delivery

Using tile scans of tissue sections with an overlay based on levels of SS from SPs constructed from the planar cut method, the influence of SS on the microdistribution of NPs in PC3 and OHS tissue was characterized.

A weakly negative correlation between NP accumulation and SS level was found for all groups except the control group of OHS tissue, where the correlation was weakly positive. A negative correlation between NP accumulation and level of SS was expected in control groups, mainly because SS has been shown to cause blood vessel collapse [13, 59] and areas with higher SS would therefore be less accessible

to NPs. The fact that the correlation found was weak indicates that this factor is present, but not crucial.

The fact that the control group of OHS tissue displayed a weakly positive correlation, while the treated group correlated negatively, could indicate that the treatment causes collapse of blood vessels in high SS areas of OHS tissue. If this is the case, it would support the hypothesis previously mentioned that the reason behind lowered SS in the treated group was a release of SS through blood vessel collapse.

In PC3 tissue, no effect of US could be found on the correlation between level of SS and NP accumulation. This could possibly be explained by the fact that PC3 tumors have a lower initial vascular density [53], and that the US treatment therefore did not significantly alter the conditions of NP accumulation in high SS areas of this tissue.

In PC3 tissue, the correlation between NP extravasation and SS level was negative for both groups. This was not the case for OHS tissue, which showed a weakly positive correlation in the treated group and no correlation in the control group. Again, a negative correlation between level of SS and NP extravasation was expected, mainly because of the higher cell density corresponding to elevated SS [13], blocking the NP's access to extravasate.

The positive correlation between NP extravasation and level of SS in the treated group of OHS tissue is probably explained by the vascular properties of OHS tissue. As mentioned, OHS tissue is well perfused throughout the tumor, but the vasculature is immature and probably more leaky than that of PC3 tissue [53]. This means that the tissue is likely to experience a greater elevation of the IFP through fluid leakage. High IFP is a well known obstacle to NP extravasation. In a scenario where MB destruction leads to a collapse of a relatively low share of blood vessels in high SS areas, and thereby lowering the SS somewhat, this could also contribute to a reduction in IFP in these areas, mainly through decompression of lymphatic vessels [59]. This would allow more NPs to extravasate from the still functioning blood vessels in the proximity, and would explain why OHS tissue in the control group showed no correlation while the treated group correlated positively.

In the treated group of OHS tissue, the extravasation was significantly lower in areas with a medium level of SS, compared to areas with a very high level of SS and areas with no SS release. In areas with no release of SS, it is likely that the extravasation was already high, because of low IFP.

Again, no effect could be seen on the correlation between level of SS and NP extravasation in PC3 tissue. With a lower baseline EPR effect, PC3 tumors would be less susceptible to lowering of IFP due to blood vessel collapse, and so this effect of the US treatment would not manifest in PC3 tissue in the same way as it did in OHS tissue.

The correlation between SS and average distance from NP to nearest blood vessel wall was negative for all groups, and a stronger negative correlation was seen for PC3 tissue. This was the expected result, as a high level of SS is partially caused by a high cell density [13], which again impairs NP transport through the ECM [53]. The higher amount of ECM components in high SS areas would probably

also contribute to lower the ability of NPs to penetrate the ECM, as the diffusion would be impaired by a crowded environment.

No effect on the correlation between ECM penetration and level of SS could be found from the US treatment in either of the tissues examined. This is an indication that the areas with a high level of SS following US treatment, still have poor conditions for NP diffusion, e.g. a high density of cells and/or ECM components. This could imply that the manner of SS release by US treatment or MB destruction is collapse of blood vessels or endothelial cells, which would not alter diffusion conditions, rather than apoptosis or collapse of HA networks, which would have that effect. On the other hand, it is also possible that the US treatment actually lowered the SS levels to such a degree that higher SS areas would become lower SS areas and therefore enable greater ECM penetration. In that case, a significant difference in the ECM penetration of the same SS level between treated and control groups would probably be visible. This is not the case for this data set, but a larger data set could possibly show this effect.

5.4 Future work

The work done in the project described in this thesis has been a contribution to a larger project involved in developing, characterizing and improving a DDS with US. This means that while some questions have been answered, it is natural and unavoidable that others have been raised. In this section, suggestions will be given as to possible paths to pursue in order to further characterize the DDS in question.

In this thesis, the DDS with US has been characterized for two different tumor models: PC3 and OHS. Previously, the same DDS has been shown to yield good results using MDA-MB-231 tumor tissue [11], and a similar DDS using US is reported promising for A431 and Bx-PC3 tissue [56]. It would be natural to characterize the microdistribution of NPs using the same methods described here for these tissues. In addition, it has been shown that the DDS described here has the potential to safely and reversibly open the blood brain barrier (BBB) [64], allowing it to be used for brain tumors. Therefore, a deeper understanding of the microdistribution of NPs in brain tumors would also be useful.

The above is also true for investigations regarding SS distribution and indeed the effect of inertial cavitation of MBs on levels of SS. Nia et al. used the planar cut method to characterize solid stress in U87, MM3V-MTC and AK4.4 tumor tissue. Stylianopoulos at al. [59] used a method preceding the planar cut method to investigate SS levels and distribution in a range of tumors. Nonetheless, SS is a parameter of tumors that has been difficult to quantify until recently, and this area of research will no doubt attract more attention in the future.

A factor which was considered in the paper by Nia et al. [13], but not accounted for here, was the stiffness of the tumors. This parameter could be measured for example by nanoindentation performed using an atomic force microscopy (AFM). Such a measurement would complement the SS measurements, as a tumor with a high degree of stiffness would release less SS than a softer tumor with the same amount of SS.

The experiments behind this thesis could prove that inertial cavitation of MBs had the effect of lowered SS in tumor tissue, but was only able to speculate as to possible reasons behind this result. It is therefore natural to wish to examine some of these reasons suggested further. First, a characterization of the amount and distribution of HA in the treated and control groups of both tumor models could easily be performed using fluorescent immunostaining. This would be able to prove if HA is affected by the treatment, and if it is responsible for the lower release of SS in the treated group.

Second, the ratio of functioning to non-functioning blood vessels in the tumor tissue should be characterized. This too can be easily performed by staining with cluster of differentiation 31 (CD31) staining and comparing to the fluorescence from lectin stained, functional blood vessels. Another approach, which is currently tested by our group, is US imaging of the vasculature using the MBs as contrast agents. By comparing the treated groups against the control groups, it can be established whether the treatment has an effect on the amount of functional blood vessels, and if blood vessel collapse can possibly explained lowered release of SS in the treated group. Here, it would be important to consider that an *elevation* of SS levels would initially cause a collapse of blood vessels, as shown by Nia et al. [13].

Finally, the role of collagen density and distribution in tumor tissue should be clarified with regards to its effect on drug delivery of NPs. Sulheim et al. [53] found no correlation between collagen density and delivery of NPs to tissue. Eggen et al. [12] could find no effect of inertial MB cavitation on collagen content. However, no analysis has been performed for this DDS with regards to collagen distribution, orientation or structure. This can be done using polarized second harmonic generation microscopy.

5.5 Clinical relevance

The ultimate goal of a DDS such as the one described in this thesis, is of course to be implemented in clinical treatment of cancer. However, the process of clinical approval is also the most important threshold for virtually all DDSs. Today, there are few DDSs based on the EPR effect of NPs that have been successful in translating to the clinic. One of the systems that have been successful in a clinical trial, is one that somewhat resembles the one described here, using free chemotherapeutics combined with stable cavitation of MBs [65], a fact which is indeed promising for the more advanced version using NPs, too.

In this thesis, important and common reasons behind difficulties with clinical translations have been investigated: NP accumulation, extravasation and ECM penetration, and inter- and intra-tumoral heterogeneity. It has been shown that this DDS has great potential in one tumor model, PC3, while perhaps being more limited in another, OHS. This information is naturally of great importance when clinical trials are to be considered. Aside from the obvious fact that the DDS is eligible only for solid tumors that are accessible to US sonication, it is important to know which types of cancer the DDS can possibly be able to treat.

Having a deeper knowledge about tumor vasculature and both it's influence on

NP drug delivery and impressionability to inertial MB cavitation, it is also possible to personalize treatment to a higher degree, an important marker for success of NP DDSs [53].

Finally, the completely novel finding that US induced MB collapse reduces the level of solid stress in tumor tissue, could possibly have a direct clinical relevance. Success in clinical trials has been shown for the reduction of SS levels by targeting collagen I and HA and in turn release forces on blood vessels to improve blood flow through the tumor and thereby increase efficiency of conventional chemotherapeutic drugs [13]. This possibility would of course depend on the reason behind the lowering of SS by inertial cavitation: if the explanation is further collapse of blood vessels, the tumor would hardly experience better perfusion by the treatment.

Chapter 6

Conclusion

The baseline EPR effect of untreated OHS tissue was found to be significantly higher than that of untreated PC3 tissue: NP accumulation was 64.9 % higher ($p=0.01$, t-test), NP extravasation was 50.3 % higher ($p<0.0001$, t-test) and ECM penetration by NPs was 35.2 % higher ($p<0.0001$, t-test) for OHS tissue. The increased NP accumulation was a result of higher blood vessel density in OHS tissue, while the increased extravasation was caused by a more immature vascular network exhibiting less continuity in the basement membrane of the vessels. NPs showed higher ECM penetration in OHS tissue in spite of diffusion limiting factors such as higher cell density here. This was probably a subsequent effect of the higher extravasation, as extravasation and ECM penetration was shown to correlate.

Treatment with US induced MB collapse could not show any significant effect on NP accumulation or ECM penetration in OHS tissue, like it did in PC3 tissue. This was in all probability due to the higher baseline EPR effect in OHS tissue.

In tumors with 6 h between injection of NPMBs and euthanization, NP extravasation was significantly decreased by 8.0 % ($p=0.002$, t-test). However, in these samples no NPs would have been present in the blood, and the measure of extravasation would be the ratio of NPs outside blood vessels to the ratio of NPs deposited along blood vessel walls or endocytosed by endothelial cells. Therefore, the reason behind the apparent decrease in extravasation was probably an effect of sonoporation and increased endocytosis of NPs by endothelial cells.

In tumors with 30 min between injection of NPMBs and euthanization, NP extravasation was significantly increased by 7.9 % ($p=0.026$, t-test). This was probably due to the effect of US induced MB collapse, which has previously been shown to increase vascular permeability.

Qualitative analysis of the distribution of SS in 30 tumor halves indicated that SS distribution is highly heterogeneous within and between tumors, and does not fit a specific distribution pattern for either OHS or PC3 tumors.

The SS release in OHS tumors was 99.5 % higher than in PC3 tumors. The result was statistically significant ($p<0.0001$, t-test). The higher levels of SS was caused by a higher density of cells and ECM components in this tissue.

Treatment with US induced MB collapse was proven to significantly reduce

the SS levels of both PC3 and OHS tissue, by 11.1 % (p=0.029, t-test) and 8.8 % (p=0.030, t-test), respectively. This is a completely novel finding. Several reasons behind the lowering of SS was hypothesized: US induced apoptosis of tumor cells, collapse of HA networks, or sonoporation and collapse of either blood vessel endothelial cells or entire blood vessel sections.

In OHS tissue, the correlation between level of SS release and NP accumulation went from positive to negative upon treatment with US. This is an indication that the treatment caused blood vessel collapse in OHS tissue, rendering high SS areas less available to NPs.

The correlation between level of SS release and NP extravasation went from non-existent to positive after US treatment in OHS tumor tissue. This too, indicates blood vessel collapse in high SS areas, inducing decompression of lymphatic vessels and thereby lowering the IFP, facilitating NP extravasation.

In PC3 tissue, treatment with US induced MB collapse did not affect the correlation between release of SS and NP accumulation, or release of SS and NP extravasation, which were both negative. A likely explanation to the difference in effect between OHS and PC3 tissue would be the lower baseline EPR effect in PC3 tissue.

The correlation between release of SS and the ability of NPs to penetrate the ECM was negative for OHS and PC3 tissue, and was not affected by US treatment or MB cavitation. This is an indication that diffusion limiting factors like cell density and HA network are not affected by US or MB cavitation, which could point to collapse of endothelial cells or blood vessels as an explanation behind lowered SS in treated groups.

Bibliography

[1] World Health Organisation. *Global Cancer Observatory*. June 20, 2018. URL: https://gco.iarc.fr.

[2] D. Ross Camidge and Duncan I. Jodrell. "Introduction to the Cellular and Molecular Biology of Cancer". In: OUP Oxford, 2005. Chap. 24 – Chemotherapy.

[3] Sun Tianmeng et al. "Engineered Nanoparticles for Drug Delivery in Cancer Therapy". In: *Angewandte Chemie International Edition* 53.46 (2014), pp. 12320–12364.

[4] Kwangjae Cho et al. "Therapeutic Nanoparticles for Drug Delivery in Cancer". In: *Clinical Cancer Research* 14.5 (2008), pp. 1310–1316.

[5] Gert Storm et al. "Surface modification of nanoparticles to oppose uptake by the mononuclear phagocyte system". In: *Advanced Drug Delivery Reviews* 17.1 (1995), pp. 31–48.

[6] Yasuhiro Matsumura and Hiroshi Maeda. "A New Concept for Macromolecular Therapeutics in Cancer Chemotherapy: Mechanism of Tumoritropic Accumulation of Proteins and the Antitumor Agent Smancs". In: *Cancer Research* 46.12 (1986), pp. 6387–6392.

[7] Hiroya Hashizume et al. "Openings between Defective Endothelial Cells Explain Tumor Vessel Leakiness". In: *The American Journal of Pathology* 156 (2000), pp. 1363–1380.

[8] William G. Pitt, Ghaleb A. Husseini, and Bryant J. Staples. "Ultrasonic Drug Delivery - A General Review". In: *Expert opinion on drug delivery* 1.1 (2004), pp. 37–56.

[9] Victor Frenkel. "Ultrasound mediated delivery of drugs and genes to solid tumors". In: *Advanced Drug Delivery Reviews* 60.10 (2008), pp. 1193–1208.

[10] Hilary A. Hancock et al. "Investigations into Pulsed High-Intensity Focused Ultrasound 2013;Enhanced Delivery: Preliminary Evidence for a Novel Mechanism". In: *Ultrasound in Medicine and Biology* 35.10 (2009), pp. 1722–1736.

[11] Sofie Snipstad et al. "Ultrasound Improves the Delivery and Therapeutic Effect of Nanoparticle-Stabilized Microbubbles in Breast Cancer Xenografts". In: *Ultrasound in Medicine & Biology* 43.11 (2017), pp. 2651–2669.

[12] Siv Eggen et al. “Ultrasound-enhanced drug delivery in prostate cancer xenografts by nanoparticles stabilizing microbubbles”. In: *Journal of Controlled Release* 187 (2014), pp. 39–49.

[13] Hadi T. Nia et al. “Solid stress and elastic energy as measures of tumour mechanopathology”. In: *Nature Biomedical Engineering* 1 (2016), p. 0004.

[14] Margaret Knowles and Peter Selby. “Introduction to the Cellular and Molecular Biology of Cancer”. In: OUP Oxford, 2005. Chap. 1 - What is Cancer?

[15] Margaret Knowles and Peter Selby. “Introduction to the Cellular and Molecular Biology of Cancer”. In: OUP Oxford, 2005. Chap. 7 – Oncogenes.

[16] Sonia Laín and David P. Lane. “Introduction to the Cellular and Molecular Biology of Cancer”. In: OUP Oxford, 2005. Chap. 8 – Tumor Supressor Genes.

[17] Douglas Hanahan and Robert A. Weinberg. “Hallmarks of Cancer: The Next Generation”. In: *Cell* 144.5 (2011), pp. 646–674.

[18] Margaret Knowles and Peter Selby. “Introduction to the Cellular and Molecular Biology of Cancer”. In: OUP Oxford, 2005. Chap. 17 – Tumour angiogenesis.

[19] Allison H. Kimberly and George W. Sledge. “Heterogeneity and Cancer”. In: *Oncology Journal* 28 (9 2014).

[20] Athanassios P. Pirentis et al. “Remodelling of extracellular matrix due to solid stress accumulation during tumour growth”. In: *Connective tissue research* 56.5 (2015), pp. 345–354.

[21] Margareth A. Knowles and P. Selby. “19 – Animal models of cancer”. In: *Introduction to the cellular and molecular biology of cancer*. OUP Oxford, 2005.

[22] Stefan Wilhelm et al. “Analysis of nanoparticle delivery to tumours”. In: *Nature Reviews Materials* (2016).

[23] Lee B. Mullin, Linsey C. Phillips, and Paul A. Dayton. “Nanoparticle Delivery Enhancement With Acoustically Activated Microbubbles”. In: *IEEE transactions on ultrasonics, ferroelectrics, and frequency control* 60 (2013).

[24] Michelle Longmire, Peter L. Choyke, and Hisataka Kobayashi. “Clearance Properties of Nano-sized Particles and Molecules as Imaging Agents: Considerations and Caveats”. In: *Nanomedicine (London, England)* 3.5 (2008), pp. 703–717.

[25] Hisataka Kobayashi, Rira Watanabe, and Peter L. Choyke. “Improving Conventional Enhanced Permeability and Retention (EPR) Effects; What Is the Apprpriate Target?” In: *Theranostics* 4.1 (2014), pp. 81–89.

[26] Donald E. Owens and Nicholas A. Peppas. “Opsonization, biodistribution, and pharmacokinetics of polymeric nanoparticles”. In: *International Journal of Pharmaceutics* 307.1 (2006), pp. 93–102.

[27] Dai Fukumura and Rakesh K. Jain. “Tumor microenvironment abnormalities: Causes, consequences, and strategies to normalize”. In: *Journal of Cellular Biochemistry* 101.4 (2007), pp. 937–949.

[28] Christian Frantz, Kathleen M. Stewart, and Valerie M. Weaver. "The extracellular matrix at a glance". In: *Journal of Cell Science* 123.24 (2010), pp. 4195–4200.

[29] Sofie Snipstad et al. "Contact-mediated intracellular delivery of hydrophobic drugs from polymeric nanoparticles". In: *Cancer Nanotechnology* 5.1 (2014), p. 8.

[30] Jeff Hardin, Gregory Bertoni, and Lewis J. Kleinsmith. "Becker's World of the Cell". In: Pearson, 2012. Chap. 12 – The Endomembrane System and Peroxisomes.

[31] Jeff Hardin, Gregory Bertoni, and Lewis J. Kleinsmith. "Becker's World of the Cell". In: Pearson, 2012. Chap. 4 – Cells and Organelles.

[32] Arun K. Iyer et al. "Exploiting the enhanced permeability and retention effect for tumor targeting". In: *Drug Discovery Today* 11.17 (2006), pp. 812–818.

[33] B. Beuscher-Willems Guenter Schmidt. "Ultrasound". In: Thieme Medical Publishers Inc., 2006. Chap. 1 – Basic Physical and Technical Principles.

[34] Ghaleb A. Husseini, William G. Pitt, and Ana M. Martins. "Ultrasonically triggered drug delivery: Breaking the barrier". In: *Colloids and Surfaces B: Biointerfaces* 123 (2014), pp. 364–386.

[35] Nadine Barrie Smith and Andrew Webb. "Introduction to Medical Imaging : Physics, Engineering and Clinical Applications". In: Cambridge: Cambridge University Press, 2010. Chap. 4 – Ultrasound imaging.

[36] William D. O'Brien. "Ultrasound–biophysics mechanisms". In: *Progress in biophysics and molecular biology* 93.1–3 (2006), pp. 212–255.

[37] Vera Paefgen, Dennis Doleschel, and Fabian Kiessling. "Evolution of contrast agents for ultrasound imaging and ultrasound-mediated drug delivery". In: *Frontiers in Pharmacology* 6 (2015), p. 197.

[38] Paul A. Dayton et al. "Application of Ultrasound to Selectively Localize Nanodroplets for Targeted Imaging and Therapy". In: *Molecular imaging* 5.3 (2006), pp. 160–174.

[39] Klazina Kooiman et al. "Acoustic behavior of microbubbles and implications for drug delivery". In: *Advanced Drug Delivery Reviews* 72 (2014), pp. 28–48.

[40] W. L. Nyborg. "Ultrasonic microstreaming and related phenomena." In: *The British Journal of Cancer. Supplement* 5 (1982), pp. 156–160.

[41] Jurek W. Dobrucki. "From Principles to Biological Applications". In: Wiley-VCH Verlag GmbH & Co. KGaA, 2013. Chap. 3.

[42] G. Ya. Wiederschain. *The Molecular Probes Handbook. A Guide to Fluorescent Probes and Labeling Technologies.* Life Technologies, 2010.

[43] Paras N. Prasad. "Introduction to Biophotonics". In: John Wiley & Sons, Inc., 2003. Chap. 7 - Bioimaging: Principles and Techniques.

[44] Nikolaus Naredi-Rainer et al. "Confocal Microscopy". In: Wiley-VCH Verlag GmbH & Co. KGaA, 2013. Chap. 5.

[45] James Wyant. “White light interferometry”. In: *Proceedings of SPIE*. 2002.

[46] Øystein Fodstad et al. “Characteristics of a cell line established from a patient with multiple osteosarcoma, appearing 13 years after treatment for bilateral retinoblastoma”. In: *International Journal of Cancer* 38.1 (1986), pp. 33–40.

[47] Ýrr Mørch et al. “Nanoparticle-stabilized microbubbles for multimodal imaging and drug delivery”. In: *Contrast Media & Molecular Imaging* 10.5 (2015), pp. 356–366.

[48] Johannes Schindelin et al. “Fiji: an open-source platform for biological-image analysis”. In: *Nat Meth* 9.7 (2012), pp. 676–682.

[49] G W Zack, W E Rogers, and S A Latt. “Automatic measurement of sister chromatid exchange frequency.” In: *Journal of Histochemistry & Cytochemistry* 25.7 (1977), pp. 741–753.

[50] TW Ridler and S Calvard. “Picture thresholding using an iterative selection method”. In: *IEEE Transaction on Systems, Man and Cybernetics* 8 (1978), pp. 639–632.

[51] Wen-Hsiang Tsai. “Moment-preserving thresolding: A new approach”. In: *Computer Vision, Graphics, and Image Processing* 29.3 (1985), pp. 377–393.

[52] J.N. Kapur, P.K. Sahoo, and A.K.C. Wong. “A new method for gray-level picture thresholding using the entropy of the histogram”. In: *Computer Vision, Graphics, and Image Processing* 29.3 (1985), pp. 273–285.

[53] Einar Sulheim et al. “Multi-modal characterization of vasculature and nanoparticle accumulation in five tumor xenograft models”. In: *Journal of Controlled Release* 279 (2018), pp. 292–305.

[54] Hyounkoo Han et al. “Effect of high intensity focused ultrasound (HIFU) in conjunction with a nanomedicines-microbubble complex for enhanced drug delivery”. In: *Journal of Controlled Release* 266 (2017), pp. 75–86.

[55] Lingxi Xing et al. “Ultrasound-Mediated Microbubble Destruction (UMMD) Facilitates the Delivery of CA19-9 Targeted and Paclitaxel Loaded mPEG-PLGA-PLL Nanoparticles in Pancreatic Cancer”. In: *Theranostics* 6.10 (2016), pp. 1573–1587.

[56] Benjamin Theek et al. “Sonoporation enhances liposome accumulation and penetration in tumors with low EPR”. In: *Thirteenth International Nanomedicine and Drug Delivery Symposium* (2016).

[57] Caitlin W. Burke et al. “Ultrasound-activated Agents Comprised of 5FU-bearing Nanoparticles Bonded to Microbubbles Inhibit Solid Tumor Growth and Improve Survival”. In: *Molecular Therapy* 22.2 (2013), pp. 321–328.

[58] I. Lentacker et al. “Understanding ultrasound induced sonoporation: Definitions and underlying mechanisms”. In: *Advanced Drug Delivery Reviews* 72 (2014), pp. 49–64.

[59] Triantafyllos Stylianopoulos et al. "Causes, consequences, and remedies for growth-induced solid stress in murine and human tumors". In: *Proceedings of the National Academy of Sciences of the United States of America* 109.38 (2012), pp. 15101–15108.

[60] Guanqing Ou and Valerie Marie Weaver. "Tumor-induced solid stress activates -catenin signaling to drive malignant behavior in normal, tumor-adjacent cells". In: *BioEssays : news and reviews in molecular, cellular and developmental biology* 37.12 (2015), pp. 1293–1297.

[61] Q Guo, LX Jiang, and B Hu. "Focused ultrasound induces apoptosis in pancreatic cancer cells". In: *Chin Med J* (2012).

[62] Bo Zhang et al. "Low-frequency low energy ultrasound combined with microbubbles induces distinct apoptosis of A7r5 cells". In: *Molecular Medicine Reports* (2014).

[63] Nobuo Suzuki et al. "Low-intensity pulsed ultrasound induces apoptosis in osteoclasts: Fish scales are a suitable model for the analysis of bone metabolism by ultrasound". In: *Comparative Biochemistry and Physiology Part A: Molecular & Integrative Physiology* 195 (2016), pp. 26–31.

[64] Habib Baghirov et al. "Ultrasound-mediated delivery and distribution of polymeric nanoparticles in the normal brain parenchyma of a metastatic brain tumour model". In: *PLoS ONE* 13.1 (2017), e0191102.

[65] Georg Dimcevski et al. "A human clinical trial using ultrasound and microbubbles to enhance gemcitabine treatment of inoperable pancreatic cancer". In: *Journal of Controlled Release* 243 (2016), pp. 172–181.

Appendix A

Image analysis: NP microdistribution in OHS tumor tissue

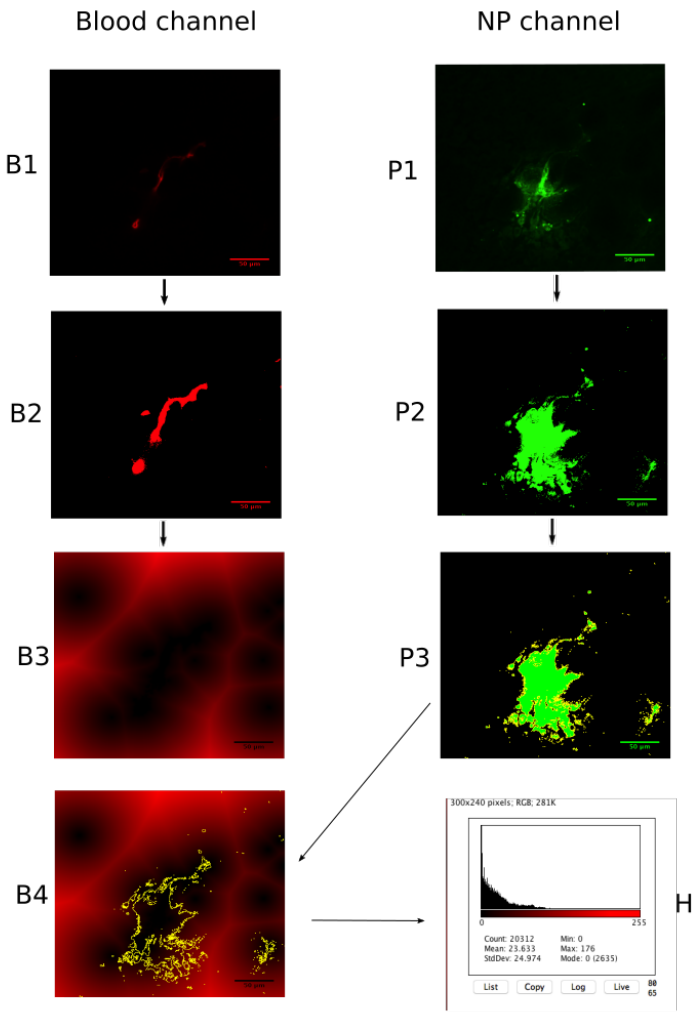

Figure A.1: Illustrated explanation of the image analysis for NP microdistribution in OHS and PC3 tumor tissue. B1 and P1: fluorescent images from the blood vessel and NP channel, respectively. B2 and P2: binary images resulting from applying a pixel threshold. B3: distance map from B2. Each pixel has been assigned the value which equals its distance (in pixels) from the blood vessel thresholded in B2. P3: the ROI is defined as the NP "cloud". B4: the ROI from P3 is overlaid on the distance map from B3. H: histogram of the pixel values inside the overlay ROI in B4. These data equal the distribution of distances between pixels defined as NPs and the blood vessel.

Appendix B

Image analysis: Solid stress

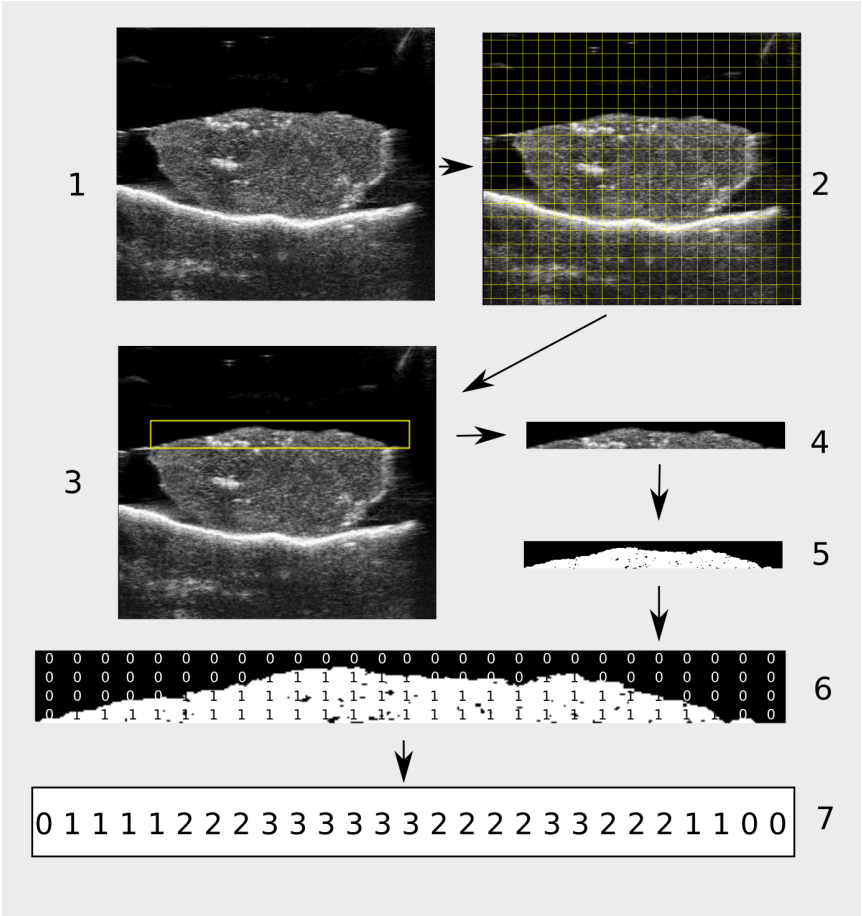

Figure B.1: Illustrated explanation of the image analysis for SS measurement in US images. 1: A stack of US images cover the entire tumor half. The gel surface is visible at both sides of the tumors. Below the tumor is a large mirror-image artifact, which does not interfere with the current analysis. 2: The stack is rotated so that the middle image is level with regards to the gel surface. A 20×20 grid is used as a visionary aid in rotating. 3: The tumor surface is marked by placing a rectangle with the lower left corner at the point where the tumor surface breaks the gel surface. Step 3 and onward is performed individually for each image in the stack. 4: Only the rectangular ROI containing the tumor surface is kept. Assuming that the original cut of the tumor was straight, this is an image of the part of the tumor that rose above the gel surface after cutting. 5: A pixel threshold is applied. 6: The image from step 5 is saved as a text image, where each black pixel is saved as the value 0, and each white pixel is saved as the value 255. (This illustration contains fewer pixels than the actual image, and the value 1 in stead of 255.) 7: A vector is constructed from the text image. The values in the vector represents the height (in pixels) which the tumor surface rises above the gel surface at each point.

Appendix C

Image analysis: Tile scans

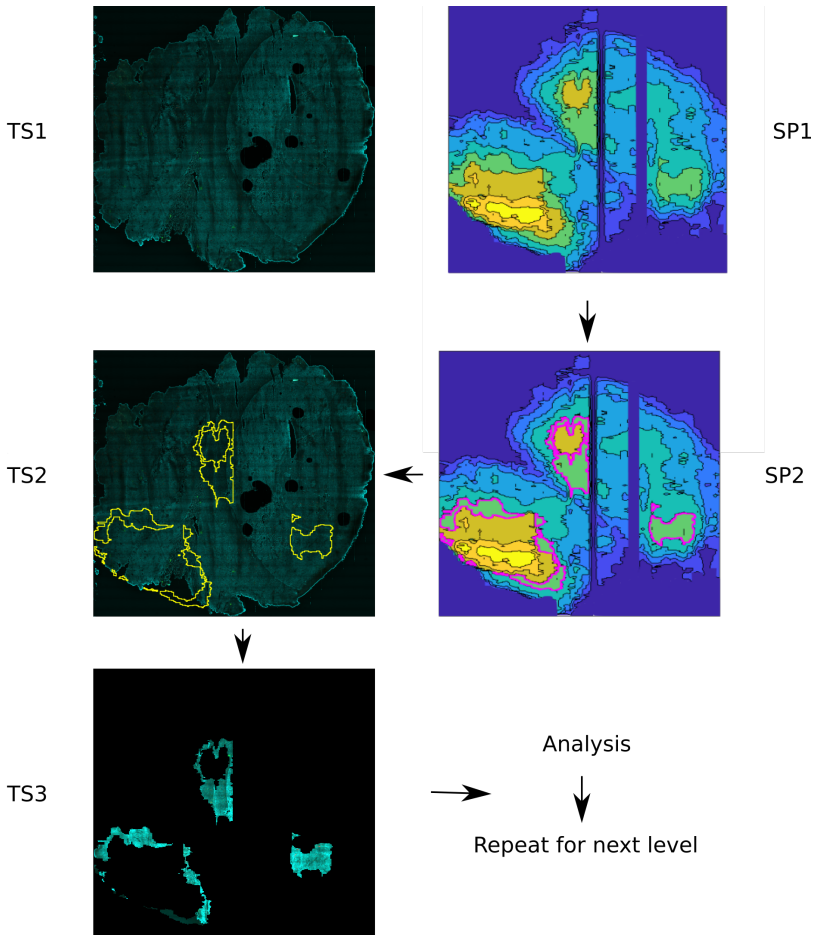

Figure C.1: Illustration of the image analysis procedure for the tile scans described in Section 3.5.3. TS1: Tile scan in three channels. SP1: SP scaled to match the size of the tile scan. SP2: All regions of one level (e.g. one color) are marked as a ROI using the "wand (tracing) tool" in FIJI. TS2: The ROI from SP2 is transferred to the tile scan. TS3: Only the areas inside the ROI is kept for analysis, everything else is cleared. The subsequent analysis is described in Appendix A. The procedure is repeated for every level (color) of the SP.

Appendix D

Image basis from planar cut method

Table D.1: Overview of the image basis from the planar cut method for measuring release of SS. Tumor halves were labelled with a number corresponding to the animal of origin, and "A" or "B". "Images" indicates the number of US images each tumor half consisted of. "Section" indicates which depth was used for the tile scan (1 is closest to the cut surface). For some tumor halves, none of the images could be used for statistical analysis due to excessive artifacts. SP indicates that a surface plot could be constructed and used for tile scan analysis.

Label	Tumor type	Group	Images	Section	Tiles
1A	OHS	Control	60	2	638
1B	OHS	Control	60	2	810
2A	OHS	Treated	0 (SP)	1	399
2B	OHS	Treated	29	1	380
3A	OHS	Treated	39	1	361
3B	OHS	Treated	32	3	182
4A	OHS	Treated	70	3	676
4B	OHS	Treated	0		
5A	OHS	Control	70	1	638
5B	OHS	Control	67	2	728
6A	OHS	Control	29	2	135
6B	OHS	Control	0 (SP)	2	104
7A	OHS	Control	57	1	700
7B	OHS	Control	54	1	504
8A	OHS	Treated	62	1	650
8B	OHS	Treated	59	1	607
9A	PC3	Treated	25		
9B	PC3	Treated	24		
10A	PC3	Control	41		
10B	PC3	Control	43		
11A	PC3	Treated	51		
11B	PC3	Treated	45		
13A	PC3	Control	33		
13B	PC3	Control	0		
14A	PC3	Treated	52		
14B	PC3	Treated	40		
15A	PC3	Control	35		
15B	PC3	Control	56		

Table D.2: Table D.1 continued.

Label	Tumor type	Group	Images	Section	Tiles
17A	PC3	Treated	59	2	644
17B	PC3	Treated	25	1	572
18A	PC3	Control	24	1	500
18B	PC3	Control	41	1	400
19A	PC3	Treated	43	2	441
19B	PC3	Treated	51	2	594
20A	PC3	Control	45	1	506
20B	PC3	Control	33	1	675
21A	PC3	Treated	41	1	756
21B	PC3	Treated	43	1	437
22A	PC3	Control	51	1	725
22B	PC3	Control	45	3	462
23A	PC3	Treated	33	2	448
23B	PC3	Treated	51	1	475
24A	PC3	Control	45	1	361
24B	PC3	Control	0		

Appendix E

Surface plots of solid stress distribution

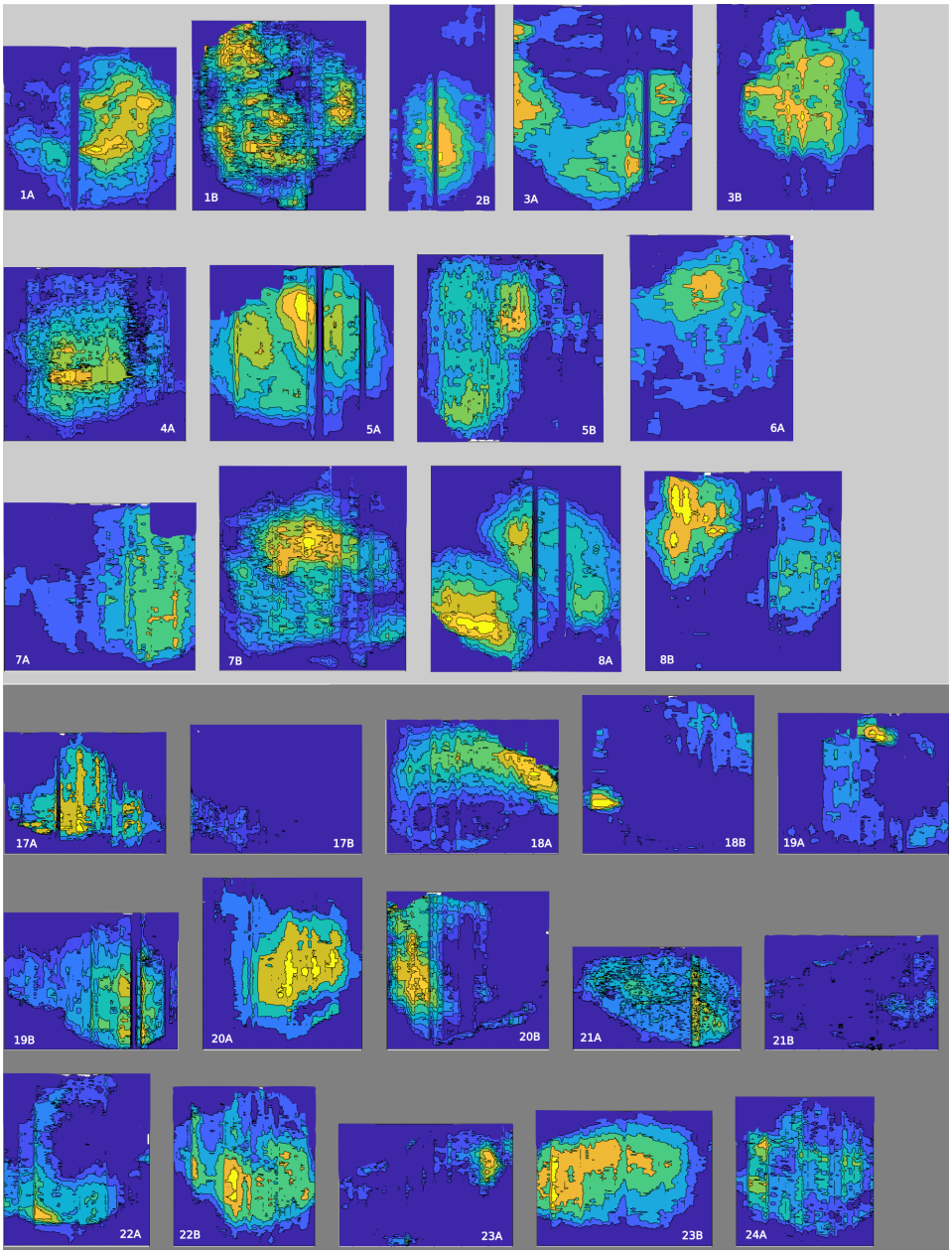

Figure E.1: SPs showing SS distribution in 28 tumor halves. Light grey background: OHS tumors. Dark grey background: PC3 tumors. Both tissue types show large heterogeneity between tumor halves.

Appendix F

Solid stress measurements: data per animal

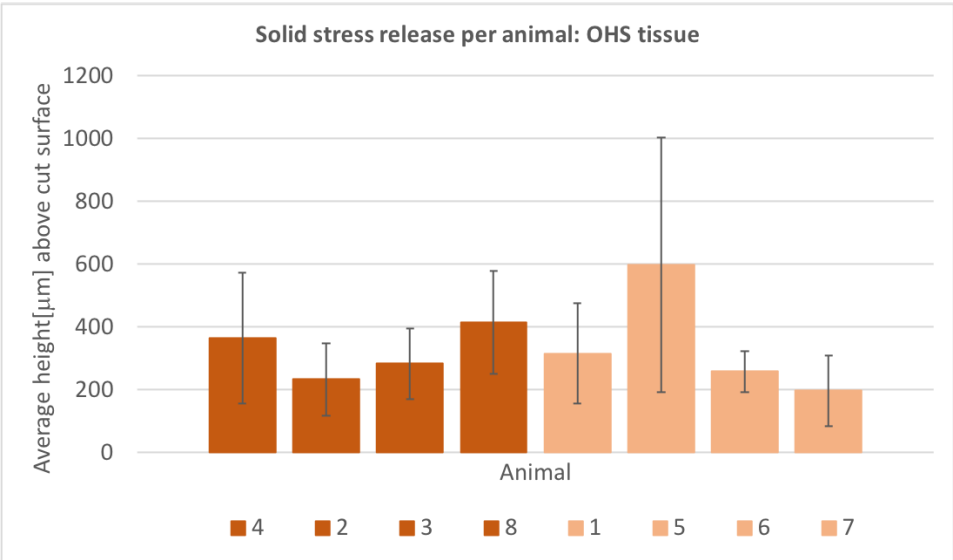

Figure F.1: Average SS release per animal in OHS tumor tissue. Error bars are SD per animal. Treated group in dark orange, control group in light orange. SS release is measured in tumor surface height [µm] above cut surface.

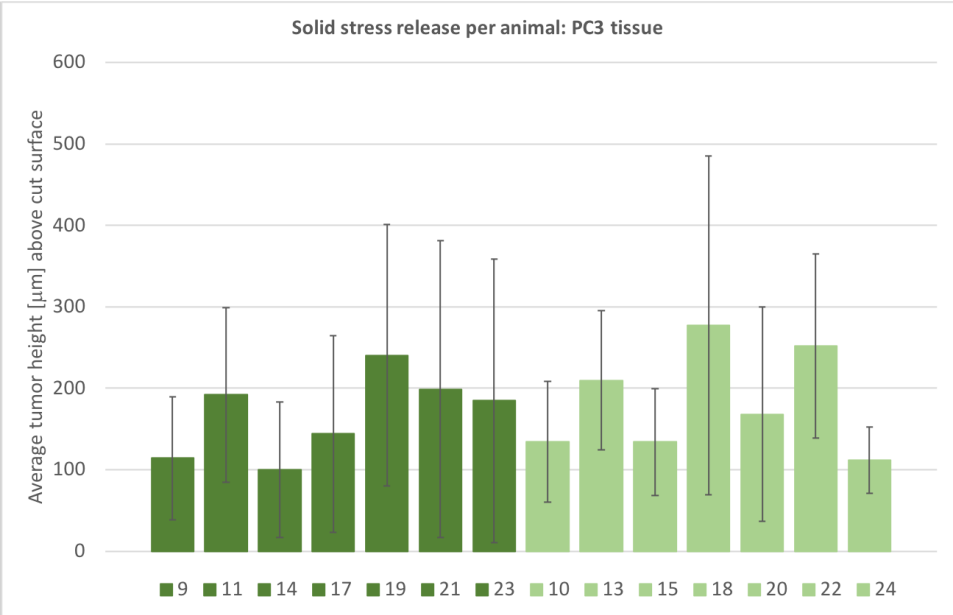

Figure F.2: Average SS release per animal in PC3 tumor tissue. Error bars are SD per animal. Treated group in dark green, control group in light green. SS release is measured in tumor surface height [µm] above cut surface.

Appendix G

NP extravasation in OHS tissue: tile scans

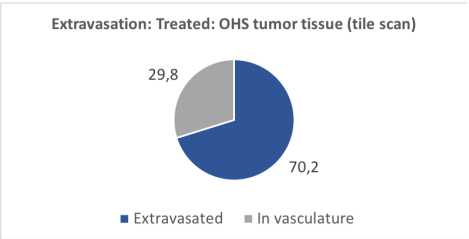

(a) Percentage of NPs inside (grey)/outside (dark blue) blood vessel in the treated group of OHS tissue. 70.2±6.2 % of the NPs were extravasated in this group

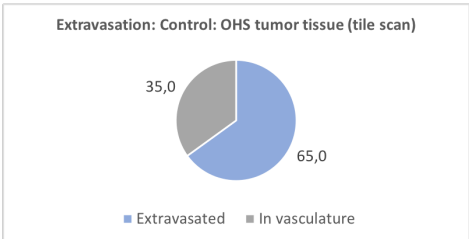

(b) Percentage of NPs inside (grey)/outside (light blue) blood vessels in the treated group of OHS tissue. 29.8±11.5 % of the NPs were extravasated in this group

Figure G.1: NP extravasation in OHS tumor tissue, based on the data acquired from image analysis of tile scans. The treated group experienced a 7.9 %, significant increase in NP extravasation compared to the control group. The p-value was 0.026.